Research Article

Plasmon-induced visible light absorption arising from edge-interfaces of titanium-oxides nanocomposites

Chaoqun Cheng, Kim R. Gustavsen, Kaiying Wang [*]

Department of Microsystems, University of South-Eastern Norway, 3184, Horten, Norway

ARTICLE INFO

ABSTRACT

The efficient utilization of visible light on wide-bandgap metal-oxides is a long-term goal but is still a grand challenge for plasmon-driven chemistry. The plasmon-induced concentration of photons in adjacent materials provides a strategic pathway to extend the light-harvesting regime to sub-bandgap. With the abundant edge-spots in surface nanostructures, here, we report that the titanium-oxides nanocomposites composed of the metallic titanium coupled with its oxides exhibit significant resonant visible absorption. The experimental characterizations with computational analyses demonstrate that the excited plasmon resonance at edge-interfaces results in the unique visible absorption band. Localized field-enhancement, charge-scattering, and hot-electrons effects conclusively confirm that the visible absorption is derived from the plasmon resonance, rather than the narrowing of bandgap or energy levels of impurities or defects. The plasmon-induced absorption effectively enhances the separation and transfer of photogenerated charge carriers leading to improved photoactivity. Our results help to advance titanium-oxides nanocomposites towards plasmonic chemistry in the visible-light region and highlight a potential general route to harnessing photons beyond the bandgap limitation based on plasmonic metal-oxides nanocomposites.

1. Introduction

Semiconducting metal oxides have been widely employed in photocatalysis thanks to the photon-captured bandgap transitions and superior electronic structures [1–4]. Extending the absorption spectrum of broad bandgap metal oxide such as TiO_2 to visible light is of critical importance for making full use of solar energy and advancing the photocatalytic applications [5–7]. Tremendous efforts have been made in engineering the low-dimensional nanoarchitectures [8,9] and tailoring the electronic structures [10–12] for visible light response. Most strategies for titanium oxide are dominated by doping with cation or anion ions [13–16], and hetero-combining with complementary semiconductors or photosensitizers [17–20]. However, these strategies are inevitably accompanied by a marked deviation of the initially appropriate electronic energy levels and a deficiency of the charge transfer characteristics. Exploring alternative pathway to extend the photons utilization scheme is therefore designed.

Plasmon resonance induced light capture at the interfaces of nanocomposites has garnered great interest because it offers an alternative route to harness light energy and advance plasmonic catalysis beyond the limitation of bandgap [21–23]. By constructing the metal-oxide nanocomposite, variation of oxide dielectrics can modulate the optical properties of the interfacial metallic surface to activate plasmon resonance that selectively enables visible absorption [24]. Plasmon resonance can further transfer the captured light energy to adjacent oxide for enhancing photoactivity through the effects of hot-charge injection, near-field amplification, light-scattering, or plasmon-induced resonance energy transfer (PRET) mechanisms [25–28]. PRET stimulates the generation of free charge carriers in adjacent materials through the non-radiative relaxation of resonance energy via dipole-dipole coupling [27]. The relaxation expands plasmonic energy transmission distance over a wider spatial range, bypassing the interface barrier and band structure restrictions.

Engineering titanium-oxides (Ti-TiO$_x$, $0 < x \leq 2$) nanocomposites composed of earth-abundant metallic Ti and its oxides (TiO$_x$) promise to support plasmon-coupled visible absorption. Earlier studies have shown that the composites of Ti–SiO$_2$ possess controllable plasmon-induced absorption in the red and near-infrared regions [29]. Recent Ti-TiO$_x$ composites have also shown some results linked to plasmon-induced absorption and near-field enhancements such as tunable visible

---

* Corresponding author.
E-mail address: Kaiying.Wang@usn.no (K. Wang).

absorption [30], interfacial dipole near-field effect [31], photothermal effect [32,33], and photon utilization above the ultraviolet wavelengths [34]. Despite these collected evidence, the underlying mechanism behind enhanced photoactivity is still not clearly understood. A thoroughly convincing validation of the plasmonic effects, which captures visible light and generates energetic charge carriers, remains elusive. The determined plasmon-induced visible absorption will be distinctive from any other factors and act as a dominant factor in developing Ti-TiO$_x$ nanocomposites that bear applications ranging from plasmonic catalysis to biochemistry.

To engineer and address plasmonic effects in Ti-TiO$_x$ nanocomposites, we have carried out theoretical and experimental studies. Nanostructured interfaces between metallic Ti and its oxides dielectrics are found to be effective in enabling plasmonic light absorption in the visible region. Abundant edge-interfaces in the surface nanostructures have been demonstrated to play a vital role in the excitation of plasmon resonance. The rich edge-interfaces exhibit strong and tunable visible absorption. Scattering-induced photocurrent enhancement, solid alignment between photoelectrochemical activity and light absorption spectrum, and generation of hot electrons unitedly ascertain that the excitation of plasmon resonance leads to the visible absorption. Our results offer a substantial validation of plasmon-induced visible absorption at the edge-interfaces of Ti-TiO$_x$ nanocomposites and highlight a potential general route to enable plasmonic absorption of visible-light, based on not only titanium-oxides but also other related metal-oxides nanocomposites.

2. Methods

2.1. Numerical simulations

Finite-element based frequency-domain methods (COMSOL Multiphysics) were used to solve the electric field distribution [35,36]. The geometries were constructed with Ti metal as substrate and TiO$_2$ nanoparticle dielectrics on the Ti substrate in the ambient atmosphere. A uniform plane-wave of transverse electric (TE) - polarized electromagnetic radiation was incident vertically on the top port. The optical constants for the materials of Ti and TiO$_2$ were taken from references, respectively [37,38]. We have simulated periodic electric field enhancement produced along the polarization direction. The computation is completed in two steps. First, the background field solution is calculated on the periodic structure of the metallic Ti film substrate without the TiO$_2$ dielectric. The metallic Ti substrate is individually set with Floquet conditions for periodic structure simulations. Second, the full-field is solved with the presence of a TiO$_2$ dielectric on the Ti substrate. The near-field and light absorption enhancements were deduced and analyzed. Please refer to the numerical calculations in the Supplementary Information (SI) for the details of the geometries and calculation parameters.

2.2. Fabrications and characterizations

Nanocomposites of Ti-TiO$_x$ on glass substrate. First, metallic Ti thin film (100 nm) was deposited on a glass substrate by electron-beam evaporation (E-beam). The second layer of TiO$_x$ thin film was deposited on the surface of metallic Ti by E-beam with a designed thickness. The as-deposited nanocomposites were followed by thermal annealing at 400 °C for 3 h in the E-beam chamber with an ultra-high vacuum.

Nanocomposites of Ti-TiO$_x$ on Si substrate. First, metallic Ti film (300 nm) on a planar Si substrate was deposited by E-beam. The nanocomposites were then sub-oxidized at the defined thermal oxidation temperatures (400, 450, 500, 550, 600, 650 °C), respectively, for 5 h in a tube furnace with a controlled flowing of oxygen gas.

Nanocomposites of Ti-TiO$_x$ nanostructures on metallic Ti foil substrate. The Ti foils, L: 20 mm × W: 14 mm × T: 0.5 mm, 99.99% purity, were cut out from the bulk Ti sheets. The Ti foils immersed in aqueous

acetone solution were rinsed by an ultrasonic bath and subsequently dried by high-pressure flowing nitrogen gas. Fabrication of the nanocomposites of the Ti-TiO$_x$ nanostructures consists of two-step processes. The nanostructures were first created on the top surface of the Ti foils via a wet chemical etching process, followed by a second thermal sub-oxidation process in a tube furnace with a controlled flow of oxygen gas.

The light absorption spectra of all the as-prepared samples were measured by Shimadzu UV–Vis 2600 spectrophotometer with default diffuse absorption settings. The spectrophotometer is equipped with an integrated sphere assembly and calibrated by standard BaSO$_4$ specimen. The BaSO$_4$ was used as a reference sample for the absorption measurements in the wavelength range of 200–850 nm with a slit width of 1 nm. Scanning electron microscope (SEM) images were obtained using Hitachi SU-8230. Bright and Dark-field optical images were captured by an optical microscope Leica DM3 XL.

2.3. Photoelectric and photoelectrochemical (PEC) characterizations

Solid-state current-voltage (I–V) data was obtained by measuring the electric current on the device in response to a given sweeping voltage stimulus in the dark and in the global illumination of a solar simulator, respectively, on a high-sensitivity electrochemical workstation (CH Model 600E Series). Time-dependent transient photocurrent responses were measured under the global illumination of solar light on the device at zero bias with a periodic chopper. During the measurements, the solid-state device of Ti-TiO$_x$ nanocomposites with contacting electrodes (metal films deposited by E-beam) was placed in a flowing nitrogen gas atmosphere at room temperature to reduce the photo-thermoelectric effect to a minimum.

PEC activities of open-circuit potential (OCP) and incident photon-to-electron conversion efficiency (IPCE) were measured on the device of Ti-TiO$_x$ nanocomposites with the electrochemical workstation of model-600E series. The device was employed as the working electrode in the three-electrode cell with 1 M KOH aqueous solution, Pt foil as the counter electrode, and Ag/AgCl with a saturated KCl solution as the reference electrode. All the potentials are reported with respect to the Ag/AgCl electrode in saturated potassium chloride electrolyte. Before each measurement, the aqueous solution was bubbled with N$_2$ for 20 min to remove dissolved gas. IR compensation was automatically carried out in the real-time measurement unless otherwise stated. The simulated solar source employed was a 500 W Xeon lamp with an AM 1.5G filter with a power density of 100 mW/cm^2.

During the OCP measurements, the device in the aqueous solution was illuminated by the AM 1.5G full-spectrum solar light. An initial steady state was obtained by placing the cell statically in the dark at room temperature for 2 h. With steady light on/off operations, the OCP data was recorded. For the IPCE measurements, the device was passivated with 2-nm Ni film on the surface. The Ni film deposited by E-beam at an ultra-low deposition rate was thermally annealed at an ultra-high vacuum in the chamber. The Ni film was employed for protecting the photoelectrode of Ti-TiO$_x$ from photo-corrosion. The IPCE measurements were carried out under the illumination of monochromatic light at the constant potential of −0.21 V. The monochromatic light is modulated and comes out from an optical monochromator that is connected with the simulated solar with a power density of 100 mW/cm^2. IPCE $(\lambda) = 1240 J/(\lambda I_{light})$, where J is the measured photocurrent density (μA/cm^2), λ is the wavelength of the incident monochromatic light (nm), and I_{light} is the measured light intensity (μW/cm^2) at the wavelength of λ [39].

3. Results and discussion

We initially built a model of Ti–TiO$_2$ composite (Fig. 1a) to probe light-matter interactions at the nanoscale, with more details included in the SI (Fig. S1). We calculated spatial field distribution as a function of wave frequencies to derive enhanced electric field and light absorption
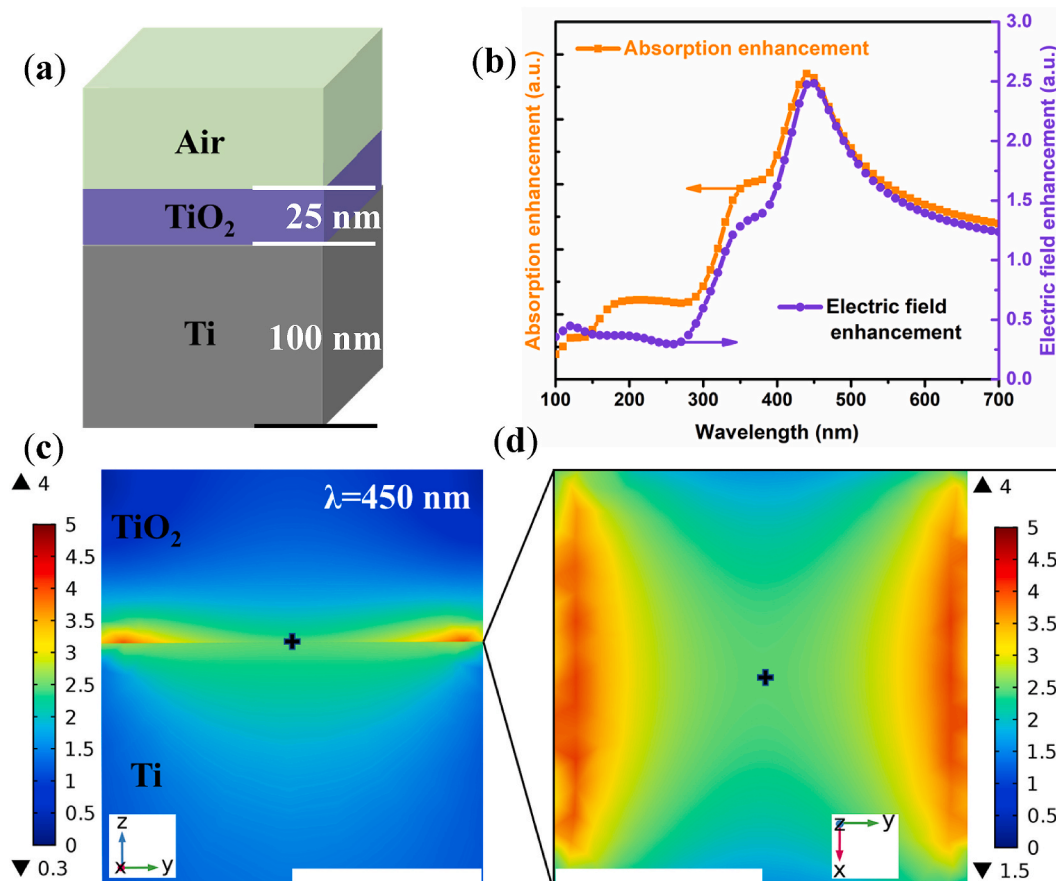
Fig. 1. (**a**) A schematic of the model of Ti–TiO$_2$ composite for numerical calculations. (**b**) The absorption spectrum of the composite and field enhancement spectrum calculated at the central point of the interface between Ti and TiO$_2$. (**c**) Vertical cross-sectional distribution of spatial electric field intensity-enhancement ($|E|/|E_0|$) in the y-z plane under the excitation of an incident TE-polarized plane wave of $\lambda = 450$ nm (inset scale bar: 25 nm). (**d**) The corresponding spatial field distribution of intensity-enhancement ($|E|/|E_0|$) in the x-y plane (inset scale bar: 25 nm). The black cross shows the location of the central point.

[35]. Fig. 1**b** presents the light absorption enhancement profile and field-intensity enhancement spectrum at the central point of the interface plane across a wide range of light wavelengths. The light absorption band centered around 450 nm aligns closely with the field enhancement profile, indicating a correlation between them. Fig. 1 **c** and **d**, which show spatial field distributions at the interface, disclose that the electric field is highly localized and distributed at the edge-interface. The spectral maximum of the enhanced field intensity (Fig. S2) is consistent with the absorption band in Fig. 1**b**. The spatial field with a varied width of the geometry is also calculated (Fig. S3), which shows the uniform field distributions. Overall, with the amplified near-field, the incident photons are concentrated explicitly at the interface, leading to an increased light absorption band in the visible region.

Near-field profiles (Fig. S4) and surface charge distributions (Fig. S5) on the surface are calculated at the wavelengths indicated by the three different peaks centered at 210 nm, 380 nm, and 450 nm, respectively, in the spectrum (Fig. 1b) [40,41]. Three potentially different plasmonic modes are revealed in the nanocomposite. Localized surface plasmon (LSP) mode where the field profile is strongly localized at the edge-interface (Figs. S4–a) is excited at around 210 nm. Surface plasmon-polariton (SPP) mode is dominant at the flat dielectric covered metal surface (Figs. S4–c), excited at around 450 nm. The field profile (Figs. S4–b) shows a third considerable hybridization of both the modes, excited at around 380 nm. These plasmon modes couple the free space light into surface plasmons, leading to the three different peaks in the calculated absorption spectrum (Fig. 1b). At 210 nm, the weak peak results from the LSP mode, which confines a spot of space light at the local area. The dominant peak at 450 nm is mainly induced by the SPP

mode resulted from the coupling of surface plasmons with incident light at specific wavelengths and wave vectors.

Dielectric thickness-dependence of absorption enhancement is evaluated by calculation (Fig. 2**a**), which shows that absorption amplitude augments gradually with sharper peak and higher intensity as the dielectric thickness increases, while the absorption peaks maintain almost at the same positions. The disclosed behaviors are reasonable, given the two-steps computations. More photons are confined on the metal surface and coupled with free electrons engaging in the resonance when increasing the dielectric thickness, resulting in the raised amplitude and narrower width. The peak position is primarily determined by the light energy required for the resonance excitation that is related to the number of free carriers [36,42]. Given an ideal metallic Ti as a substrate, the amount of free electrons at the domain is constant and little influenced by the dielectric thickness. The resonance energy of the light wavelength is virtually unchanged, except for the slight red-shift which is ascribed to the excited SPP mode. SPP mode is strongly interacting with electromagnetic waves and sensitive to the active dielectric thickness. When the dielectric thickness is increasing, the refractive index of the dielectric side on the surface is elevated, leading to a red shift in surface plasmon wavelength. Thus, incident photons are harvested by the plasmon resonance of Ti metal that associates with enhanced field distribution, and the TiO$_2$ dielectric mainly assists the confinement of photons at the interface for plasmon resonance.

To verify the enhanced absorption, we fabricated Ti-TiO$_x$ thin-film composites. The thin films were deposited on the glass substrates by E-beam, followed by thermal annealing. X-ray diffraction (XRD) patterns of the composites display the sharp peaks that could be assigned to
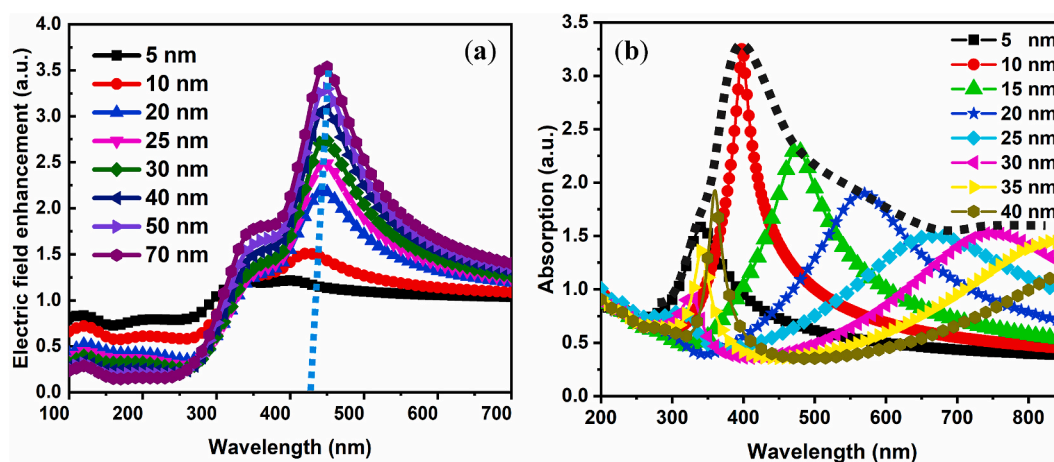
Fig. 2. (**a**) Calculated absorption enhancement spectra on the modelled Ti–TiO₂ composites. The TiO₂ is at a designed thickness. (**b**) Experimental absorption spectra on the as-prepared Ti-TiOₓ composites. The TiOₓ dielectric is at a defined thickness in the experiments, while the thickness of the metallic Ti substrate is fixed at 100 nm. The short-dashed line fits a profile of the absorption band over the experimental absorption peaks. It is noted that the peak above 850 nm in the absorption spectrum for 40 nm dielectric is not shown and observed, due to a limited wavelength scale (200–850 nm) with the UV–Vis photo-spectrometer.

the polycrystalline TiOₓ and the metallic Ti materials (Fig. S6). Optical absorption spectra at defined dielectric thicknesses are displayed in Fig. 2b. The spectra show periodic absorption peaks, attributable to the interference of multiple reflections within the high refractive-index TiOₓ dielectric layers coupled with the reflection phase at the Ti-TiOₓ interface [43–45], as observed in the interference waves of the as-prepared TiOₓ dielectric film directly deposited on glass (Fig. S7). The interference absorption peaks are red-shifted due to the increased thickness of

the TiOₓ dielectric [43,46]. The absorption peaks in the wavelength range of 400–500 nm are surprisingly sharper with higher intensity. It is noted that the absorption spectrum is a result of optical measurement on the restricted-site of the loaded sample in the spectrophotometer. A numerical spectrum is fitted over the absorption peaks (inset short-dashed line), revealing a prominent absorption band to overview the whole absorption picture. This fitted absorption band is in line with the calculated enhanced absorption profile in Fig. 2a, indicating that the
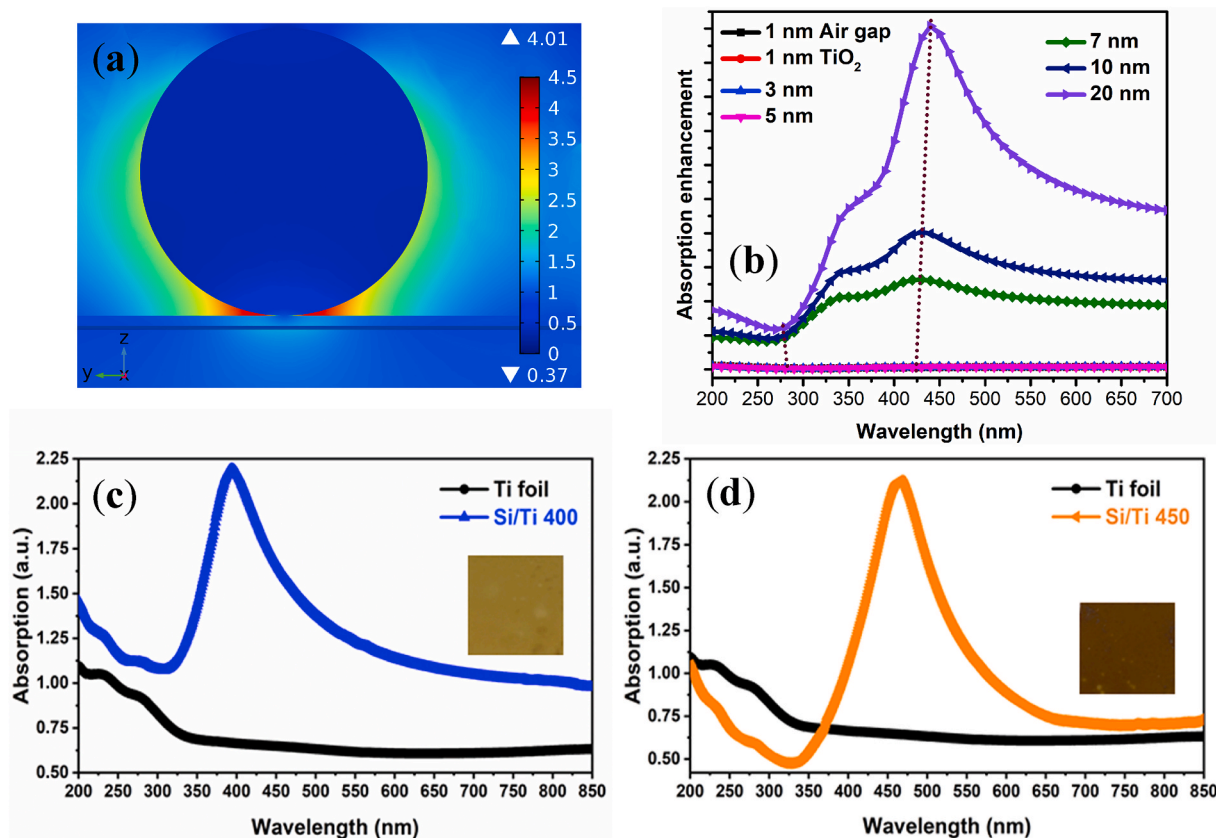

Fig. 3. (**a**) Spatial field distribution calculated at the interface under the light irradiation of 430 nm, with a nanoparticle of TiO₂ (diameter: 20 nm) placed on the surface of TiO₂ dielectric film (thickness: 1 nm) above the metallic Ti substrate. (**b**) Spectral absorption calculated under the increased thickness of the TiO₂ film. (**c-d**) Experimental absorption spectra of Ti-TiOₓ thin-film composites on Si. (**c**: 400 °C; **d**: 450 °C). The insets are bright-field images. Absorption spectra of original pure metallic Ti foil are added as a reference.

experimental absorption band in the 400–500 nm range has an additional plasmonic attribute. The appearance of plasmon and interference attributes can be explained by a coupling between plasmons and partial waves of interference [47]. Plasmon resonance can be excited at the edge-interfaces of film composites and interact with interference waves. The interaction promotes the coupling of interference waves with resonant plasmons, resulting in a sharper peak with higher amplitude in the periodic absorption band.

This plasmonic optical interference induced light absorption would be additional evidence to support the thin film composites of titanium-oxides as a visible light energy capturer. To minimize the impact of interference and create more edge-interfaces for concentrating incident photons, we have calculated near-field distributions with an additional introduction of TiO_2 dielectric nanoparticle in the model, more details in the SI (Figs. S8–S12). Fig. 3 **a** and **b** show the calculated spatial field distribution at the interface and absorption enhancement with the increased thickness of the TiO_2 dielectric film. At the edge-interface between the nanoparticle and substrate, the spatial near-field is highly amplified under the specific light irradiation ($\lambda = 430$ nm) (Fig. 3**a**, Fig. S9). The enlarged electric field intensely confines photons at the interface (Fig. 3**a**, Figs. S10–S12) and consequently raises the light absorption (Fig. 3**b**), while the positions of absorption peaks are preserved at around 450 nm. Although the introduced surface nanoparticle improves light absorption, the absorption at a varied dielectric film thickness almost follows the same trend as the absorption without nanoparticle. The features disclose that the edge-interfaces added by surface nanoparticles could focus more light on the interface. The calculated results consistently reveal that the surface plasmons of metallic Ti primarily determines the plasmonic absorption properties, and the TiO_x dielectrics help to adjust appropriate momentum to couple light in the composites.

We fabricated Ti-TiO_x thin-film composites by sub-oxidation of the Ti foils (Fig. S13). XRD patterns were measured on the as-prepared composites (Fig. S14), which shows the weak peaks of TiO_2, indicating the

formation of the Ti-TiO_x composites. Fig. 3 **c** and **d** plot the absorption spectra with the optical bright-field images of the composites. The temperature-tuned visible absorptions are magnified on amplitude with peak bands in the 300–500 nm range that aligns with the calculated absorbed band. The scattering colors in the optical dark-field images (Fig. S15 **a** and **b**) are consistent with the absorbed light wavelength. With higher thermal oxidation temperatures, the interference waves are gradually prominent in the absorption bands due to the variation of surface dielectric properties (Fig. S15 **c, d, e,** and **f**). We attribute the strong resonant absorption (Fig. 3 **c** and **d**) to a critical state in which surface plasmons are intensely oscillating in resonance with electromagnetic waves. The surface dielectrics induced interference effect is suppressed to a large extent after the low-temperature sub-oxidation. The behaviors suggest that the proper thermal temperature is advisable to well-functioning plasmonic Ti-TiO_x composites.

We further prepared nanocomposites of Ti-TiO_x nanostructures on metallic Ti foils (Fig. 4). Crystalline nano-architectures were firstly developed on the top-surface by chemical etching. Thermal sub-oxidation was then used to form the nanocomposites of Ti-TiO_x [48]. Indeed, SEM images show that the nanoscale quasi-prisms were constructed on the surface after the etching (Fig. 4**a-I**, Fig. S16). Surface and cross-sectional elemental analysis by SEM and X-ray photoelectron spectroscopy (Figs. S17 and S18) and XRD patterns (Fig. S19) further show that the TiO_x dielectrics are formed on the surface with the TiO_2 on the top-surface. The quasi-prisms expand the density of interface-edges, allowing for the amplified localization of photons at the nanoscale regions as hot-spots for plasmon resonance [49]. Light-matter interactions are strengthened by the magnified amplitude at these hot-spots, as shown in the optical dark-filed image (Fig. S20). The absorption spectrum displays a strong resonant visible absorption band around 470 nm (Fig. 4**a-II**), which agrees with the above absorption spectra from plasmon resonance.

To explore photocurrent features from the absorbed photons, we have measured the nanocomposite as a solid-state photodetector device
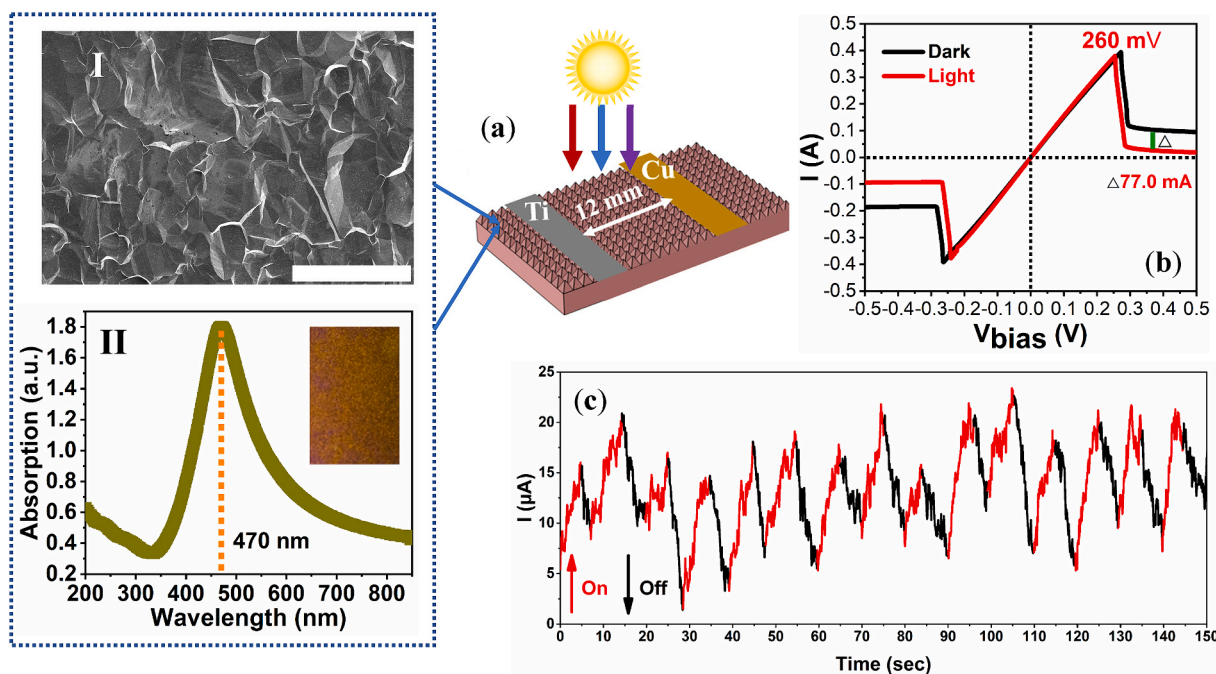

Fig. 4. Solid-state optoelectronic characterizations of the Ti-TiO_x nanocomposites. (**a**) Schematic diagram of the device of the nanocomposites with surface nanostructures. The device is covered with asymmetric metal electrodes (Ti and Cu) for generating current under the simulated solar irradiation with a power density of 100 mW/cm^2. SEM image shows the surface morphology (**I**, inset scale bar: 100 μm) and absorption spectra (**II**, inset is an optical bright-field image of the as-measured specimen). (**b**) I–V characteristic between the electrodes. (**c**) Time-dependent photocurrent spectrum in response to the global solar illumination with a controlled periodic chopper. The photo-thermoelectric effect was reduced to a minimum by keeping the device at room temperature in a flowing nitrogen gas atmosphere.

(Fig. 4a). In the model, two asymmetric metal electrodes were deposited on the surface. The asymmetric electrodes were used to drive the overall current generation through the plasmon-enhanced near-field oscillation and scattering effects [50,51]. The I–V curves (Fig. 4b) disclose the ohmic-contact characteristics within a threshold potential of 260 mV. The device also shows rectifying behaviors with a transient current offset of 77 mA at the forward/reverse bias above the threshold potential under illumination. This offset might be due to the ultra-fast recombination processes of electrons and holes and charge carriers trapped in surface dielectrics. Fig. 4c depicts a time-dependent photo-responsive current at the zero bias, with a mechanical chopper (0.2 Hz) in front of the global illumination. The photo-response current spectrum exhibits the same frequency as the chopper, indicating that the on-and-off switching operations result from the periodic illumination. The reciprocating spikes are attributed to the interactions between the charge carriers with low mobility and lifetime when transporting through the surface dielectrics, accompanied by recombination processes [52,53]. Also, due to the low carrier transport, a moderate photo-responsivity is presented with a baseline drifting. In the I–V curves, the photocurrent is identical to the dark current at a bias below the threshold potential. However, a magnified current by light illumination is obtained in the photoresponse spectrum (Fig. 4c) at room temperature. The enlarged photocurrent is ascribed to the improved charge carriers dynamics due to the charge-scattering effect induced by the plasmon resonance.

PEC characterizations were conducted using the Ti-TiO$_x$ nanocomposite as a working electrode in a three-electrode PEC cell. When the working electrode is immersed in an electrolyte solution, a balance of the Fermi energy level is initially establishing until a steady-state built at the interface between the working electrode and liquid electrolyte, which forms a stable built-in electric field with an energy band-bending. Upon illumination, the built-in electric field drives the separation and transportation of charge carriers. Simultaneously, the Fermi equilibration is established with an accumulation of holes or electrons, expressed with the V$_{oc}$ increasing or decreasing. Thus, monitoring the behaviors change of V$_{oc}$ can be used as a method for detecting features of photo-excited charge carriers [54,55]. Fig. 5a plots the V$_{oc}$ of the working electrode as a function of time. Before the light turns on, a steady potential V$_{oc}$ of −220 mV was acquired by statically placing the cell in a dark environment at room temperature for 2 h. Upon illumination, the V$_{oc}$ immediately shifts to about −570 mV, a significant photovoltage of 350 mV eventually established and sustained over 100 s at a steady state. The photovoltage effect with the negative offset provides evidence that the free charge carriers are excited by the illumination and contribute to the open potential.

The transient current response was assessed by measuring the IPCE on the nanocomposite photoelectrode (Fig. S21) [55–57]. Fig. 5b shows that the IPCE spectrum faithfully follows the visible absorption profile.
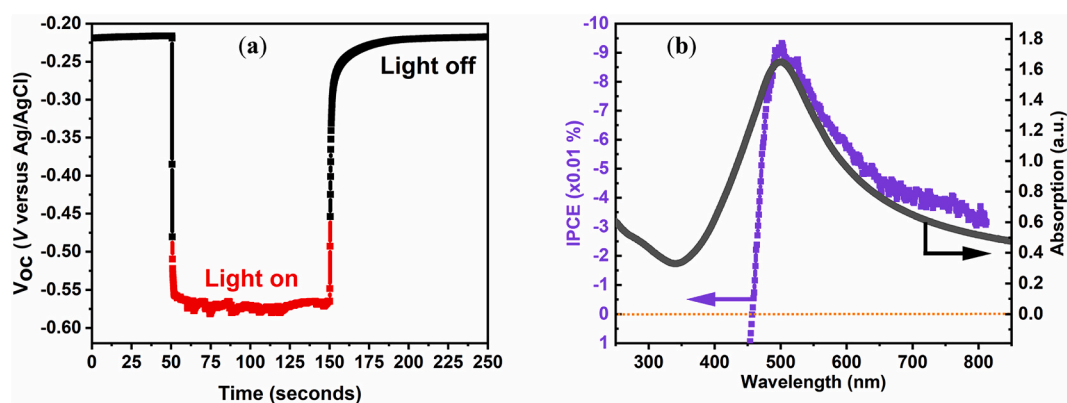
The negative-sign current points out that the free electrons are involved in the photochemical reduction reactions. Otherwise, the photochemical activity of oxidation reactions would lead to the current with a positive-sign. The alignment between the IPCE and the absorption spectrum suggests that the hot electrons are excited by the plasmon-coupled visible light. The plasmon-induced hot electrons activate the reduction reactions. The identified generation of hot electrons confirms that the plasmon resonance is excited by the incident light. The PEC characteristics conclusively support that the resonant visible absorption results from the plasmon resonance.

Other factors such as energy-levels of impurities [11,12], defects [58, 59], or narrowing of bandgap [60,61] may absorb the visible light and give rise to enhanced photocatalytic oxidation reactions. However, in contrast to the oxidation activity, the reduction reactions are observed on the visible catalytic activity (Fig. 5b), which excludes the other possible factors responsible for the visible absorption except for the interference effect. Interference waves may occur in an ultra-thin TiO$_x$ dielectric film on smooth and rough Ti metal substrates [62,63]. The interference of partial waves coupled with the resonant plasmons might contribute a little to the absorption, even though the interference has been minimized by creating the surface nanostructures.

4. Conclusions

In summary, we have demonstrated the pivotal role of the edge-interfaces on various forms of Ti-TiO$_x$ nanocomposites in exciting the high-performance plasmon resonance that exhibits a strong visible absorption band. The abundant hot-spots at the nanostructured edge-interfaces enable and facilitate the excitation of plasmon resonance associated with the localized field enhancement and light concentration. With the functional characterizations and substantial demonstrations of the Ti-TiO$_x$ nanocomposites, the plasmon-induced visible light absorption is confirmed. Taking together with the outstanding characteristics, including the periodic photo-responsivity, the significant photovoltage, and the active photochemical reactions, the further exploitation of titanium-oxides with plasmonic visible absorption can be expected for plasmonic chemistry. The nanoscale metals intensely coupled with their oxides through sub-oxidation could act as a universal solution to develop plasmonic metal-oxides nanocomposites, not only for titanium material but also for other related metallic materials.

CRediT authorship contribution statement

Chaoqun Cheng: Conceptualization, Formal analysis, Writing - original draft, co-conceived the project and the conceptual idea. designed and performed the numerical calculations and experiments, derived and analyzed the computational and experimental results. wrote

Fig. 5. PEC characterizations of the as-prepared Ti-TiO$_x$ nanocomposite as photoelectrode. (**a**) Chronopotentiometry of the OCP (V$_{oc}$) under solar light irradiation on the photoelectrode. (**b**) IPCE spectrum of the photoelectrode at a function of the light wavelengths. The visible absorption spectrum of the Ti-TiO$_x$ nanocomposite is plotted for comparison.

the paper with input from all authors. **Kim R. Gustavsen:** contributed to the interpretation of optical results. **Kaiying Wang:** Conceptualization, co-conceived the project and the conceptual idea.

Declaration of competing interest

The authors declare that they have no known competing financial interests or personal relationships that could have appeared to influence the work reported in this paper.

Acknowledgment

Appendix A. Supplementary data

Supplementary data to this article can be found online at https://doi.org/10.1016/j.optmat.2021.110847.

References

[1] S. Link, D.J. Masiello, Chem. Rev. 118 (2018) 2863–2864.
[2] M. Dhiman, J. Mater. Chem. A 8 (2020) 10074–10095.
[3] K. Sivula, R. van de Krol, Nat. Rev. Mater. 1 (2016).
[4] C. Liu, Q. Zhang, W. Hou, Z. Zou, Solar RRL 4 (2020).
[5] R. Medhi, M.D. Marquez, T.R. Lee, ACS Appl. Nano Mater. 3 (2020) 6156–6185.
[6] Z. Zhang, C. Zhang, H. Zheng, H. Xu, Acc. Chem. Res. 52 (2019) 2506–2515.
[7] Y. Noguchi, Y. Taniguchi, R. Inoue, M. Miyayama, Nat. Commun. 11 (2020) 966.
[8] I. Concina, Z.H. Ibupoto, A. Vomiero, Adv. Energy Mater. 7 (2017).
[9] M.P. Browne, Z. Sofer, M. Pumera, Energy Environ. Sci. 12 (2019) 41–58.
[10] G. Wang, Y. Yang, D. Han, Y. Li, Nano Today 13 (2017) 23–39.
[11] Y. Yang, L.C. Yin, Y. Gong, P. Niu, J.Q. Wang, L. Gu, X. Chen, G. Liu, L. Wang, H. M. Cheng, Adv. Mater. 30 (2018).
[12] T. Wu, P. Niu, Y. Yang, L.C. Yin, J. Tan, H. Zhu, J.T.S. Irvine, L. Wang, G. Liu, H. M. Cheng, Adv. Funct. Mater. 29 (2019).
[13] Y. Liu, W. Wang, X. Xu, J.-P. Marcel Veder, Z. Shao, J. Mater. Chem. A 7 (2019) 7280–7300.
[14] Z. Xiu, M. Guo, T. Zhao, K. Pan, Z. Xing, Z. Li, W. Zhou, Chem. Eng. J. (2020) 382.
[15] E. Lee, C. Park, D.W. Lee, G. Lee, H.-Y. Park, J.H. Jang, H.-J. Kim, Y.-E. Sung, Y. Tak, S.J. Yoo, ACS Catal. 10 (2020) 12080–12090.
[16] H. Tanaka, T. Uchiyama, N. Kawakami, M. Okazaki, Y. Uchimoto, K. Maeda, ACS Appl. Mater. Interfaces 12 (2020) 9219–9225.
[17] C.V. Reddy, K.R. Reddy, N.P. Shetti, J. Shim, T.M. Aminabhavi, D.D. Dionysiou, Int. J. Hydrogen Energy 45 (2020) 18331–18347.
[18] X. Pan, D. Li, Y. Fang, Z. Liang, H. Zhang, J.Z. Zhang, B. Lei, S. Song, J. Phys. Chem. Lett. 11 (2020) 1822–1827.
[19] H. Masai, H. Sakurai, A. Koreeda, Y. Fujii, T. Ohkubo, T. Miyazaki, T. Akai, Sci. Rep. 10 (2020) 11615.
[20] D.M. Tobaldi, L. Lajaunie, M. LÃ³pez Haro, R.A.S. Ferreira, M. Leoni, M.P. Seabra, J.J. Calvino, L.D. Carlos, J.A. Labrincha, ACS Appl. Energy Mater. 2 (2019) 3237–3252.
[21] J. Prakash, S. Sun, H.C. Swart, R.K. Gupta, Appl. Mater. Today 11 (2018) 82–135.
[22] S.W. Hsu, A.L. Rodarte, M. Som, G. Arya, A.R. Tao, Chem. Rev. 118 (2018) 3100–3120.
[23] X. Liu, J. Iocozzia, Y. Wang, X. Cui, Y. Chen, S. Zhao, Z. Li, Z. Lin, Energy Environ. Sci. 10 (2017) 402–434.
[24] H. Robatjazi, H. Zhao, D.F. Swearer, N.J. Hogan, L. Zhou, A. Alabastri, M. J. McClain, P. Nordlander, N.J. Halas, Nat. Commun. 8 (2017) 27.
[25] M.L. Brongersma, N.J. Halas, P. Nordlander, Nat. Nanotechnol. 10 (2015) 25–34.
[26] P.V. Kumar, T.P. Rossi, D. Marti-Dafcik, D. Reichmuth, M. Kuisma, P. Erhart, M. J. Puska, D.J. Norris, ACS Nano 13 (2019) 3188–3195.
[27] S.K. Cushing, J. Li, F. Meng, T.R. Senty, S. Suri, M. Zhi, M. Li, A.D. Bristow, N. Wu, J. Am. Chem. Soc. 134 (2012) 15033–15041.
[28] S.K. Cushing, J. Li, J. Bright, B.T. Yost, P. Zheng, A.D. Bristow, N. Wu, J. Phys. Chem. C 119 (2015) 16239–16244.
[29] J.P. Zhao, Z.Y. Chen, X.J. Cai, J.W. Rabalais, J. Vac. Sci. Technol. 24 (2006).
[30] C. Cheng, G. Liu, K. Du, G. Li, W. Zhang, S. Sanna, Y. Chen, N. Pryds, K. Wang, Appl. Catal. B Environ. 237 (2018) 416–423.
[31] S.M. Wu, X.L. Liu, X.L. Lian, G. Tian, C. Janiak, Y.X. Zhang, Y. Lu, H.Z. Yu, J. Hu, H. Wei, H. Zhao, G.G. Chang, G. Van Tendeloo, L.Y. Wang, X.Y. Yang, B.L. Su, Adv. Mater. 30 (2018), e1802173.
[32] S.I. Nikitenko, T. Chave, C. Cau, H.-P. Brau, V. Flaud, ACS Catal. 5 (2015) 4790–4795.
[33] J. Yan, P. Liu, C. Ma, Z. Lin, G. Yang, Nanoscale 8 (2016) 8826–8838.
[34] Y. Pihosh, I. Turkevych, K. Mawatari, N. Fukuda, R. Ohta, M. Tosa, K. Shimamura, E.G. Villora, T. Kitamori, Nanotechnology 25 (2014) 315402.
[35] R.A. Pala, J. White, E. Barnard, J. Liu, M.L. Brongersma, Adv. Mater. 21 (2009) 3504–3509.
[36] T. Hutter, F.M. Huang, S.R. Elliott, S. Mahajan, J. Phys. Chem. C 117 (2013) 7784–7790.
[37] T. Siefke, S. Kroker, K. Pfeiffer, O. Puffky, K. Dietrich, D. Franta, I. OhlÃdal, A. Szeghalmi, E.-B. Kley, A. TÃ¼nnermann, Adv. Optic. Mater. 4 (2016) 1780–1786.
[38] W.S.M. Werner, K. Glantschnig, C. Ambrosch-Draxl, J. Phys. Chem. Ref. Data 38 (2009) 1013–1092.
[39] Z. Yi, J. Ye, N. Kikugawa, T. Kako, S. Ouyang, H. Stuart-Williams, H. Yang, J. Cao, W. Luo, Z. Li, Y. Liu, R.L. Withers, Nat. Mater. 9 (2010) 559–564.
[40] W. Park, Nano Convergence (2014) 1.
[41] R.E. Armstrong, J.C. van Liempt, P. Zijlstra, J. Phys. Chem. C 123 (2019) 25801–25808.
[42] J.M. Luther, P.K. Jain, T. Ewers, A.P. Alivisatos, Nat. Mater. 10 (2011) 361–366.
[43] M.V. Diamanti, B. Del Curto, M. Pedeferri, Color Res. Appl. 33 (2008) 221–228.
[44] M.A. Kats, R. Blanchard, P. Genevet, F. Capasso, Nat. Mater. 12 (2013) 20–24.
[45] K.M. ęcka, M.R. Wójcik, A.J. Antończak, Math. Probl Eng. (2017) 1–11, 2017.
[46] L. Skowronski, A.A. Wachowiak, A. Grabowski, Appl. Surf. Sci. 388 (2016) 731–740.
[47] D. Choi, C.K. Shin, D. Yoon, D.S. Chung, Y.W. Jin, L.P. Lee, Nano Lett. 14 (2014) 3374–3381.
[48] Y. Horio, Y. Hara, Y. Yamamoto, Y. Morimoto, T. Naitoh, Jpn. J. Appl. Phys. 51 (2012).
[49] H. Yu, Y. Peng, Y. Yang, Z.-Y. Li, NPJ Comput. Mater. 5 (2019).
[50] A. Hohenau, J.R. Krenn, J. Beermann, S.I. Bozhevolnyi, S.G. Rodrigo, L. Martin-Moreno, F. Garcia-Vidal, Phys. Rev. B 73 (2006).
[51] Y. Liu, R. Cheng, L. Liao, H. Zhou, J. Bai, G. Liu, L. Liu, Y. Huang, X. Duan, Nat. Commun. 2 (2011) 579.
[52] T. Matsui, Y. Li, M.-H.M. Hsu, C. Merckling, R.F. Oulton, L.F. Cohen, S.A. Maier, Adv. Funct. Mater. 28 (2018).
[53] J. Gosciniak, F.B. Atar, B. Corbett, M. Rasras, Sci. Rep. 9 (2019) 6048.
[54] J. Kamimura, P. Bogdanoff, M. Ramsteiner, P. Corfdir, F. Feix, L. Geelhaar, H. Riechert, Nano Lett. 17 (2017) 1529–1537.
[55] J.S. DuChene, G. Tagliabue, A.J. Welch, W.H. Cheng, H.A. Atwater, Nano Lett. 18 (2018) 2545–2550.
[56] S. Mubeen, J. Lee, N. Singh, S. Kramer, G.D. Stucky, M. Moskovits, Nat. Nanotechnol. 8 (2013) 247–251.
[57] G. Tagliabue, J.S. DuChene, A. Habib, R. Sundararaman, H.A. Atwater, ACS Nano (2020) 5788–5797.
[58] V.N. Kuznetsov, N. Serpone, J. Phys. Chem. B 110 (2006) 25203–25209.
[59] Q. Li, J.K. Shang, Environ. Sci. Technol. 43 (2009) 8923–8929.
[60] S. Ohkoshi, Y. Tsunobuchi, T. Matsuda, K. Hashimoto, A. Namai, F. Hakoe, H. Tokoro, Nat. Chem. 2 (2010) 539–545.
[61] H. Tong, N. Umezawa, J. Ye, Chem. Commun. (Camb.) 47 (2011) 4219–4221.
[62] M.A. Kats, F. Capasso, Appl. Phys. Lett. 105 (2014).
[63] M.A. Kats, F. Capasso, Laser Photon. Rev. 10 (2016) 735–749.

Supplementary Information

Plasmon-induced visible light absorption arising from edge-interfaces of titanium-oxides nanocomposites

Chaoqun Cheng, Kim R. Gustavsen, and Kaiying Wang*

Department of Microsystems, University of South-Eastern Norway, 3184 Horten, Norway.

* E-mail: Kaiying.Wang@usn.no

Numerical calculations

A model consisting of a top TiO₂ thin dielectric and bottom Ti metal substrate was built using commercially available COMOSL Multiphysics, by using metallic Ti film as the substrate and TiO₂ dielectric in an ambient air atmosphere on the substrate. A uniform plane transverse electric (TE) - polarized electromagnetic wave was incident on the model up-port. A full field solution of the model without TiO₂ film was calculated as an expression of the background field. Finite-element based numerical calculations in the frequency domain were carried out to investigate the field distributions and near-field enhancement induced by the excitation of surface plasmons polaritons and further the optical light absorption enhancement.
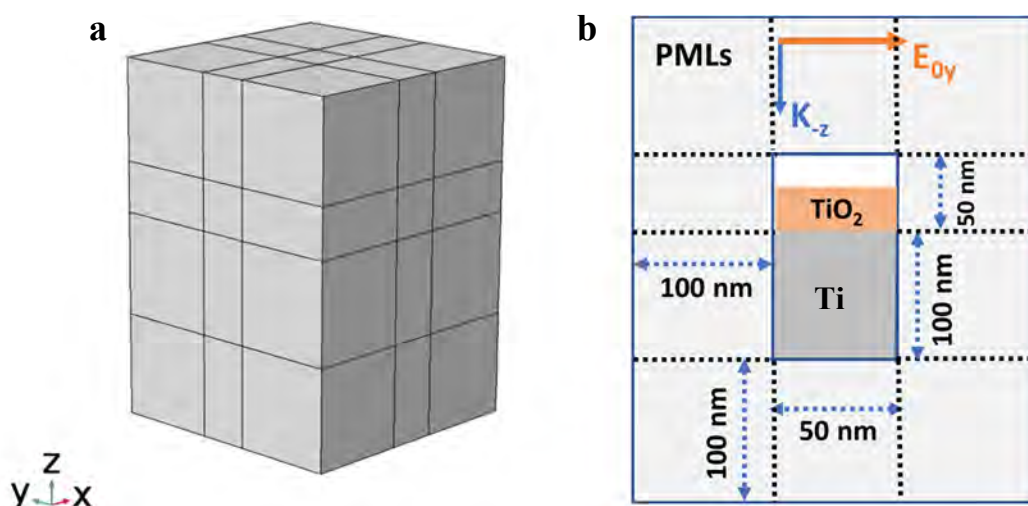
Fig. S1. Nanocomposite model of TiO₂ thin-film dielectric on Ti metal film substrate. (**a**) The 3-dimensional model under study. (**b**) Cross-section of the model with PMLs. The incident electromagnetic field with TE polarization in y-direction at the upper port propagates towards negative z-direction. The thickness of the Ti film substrate is fixed to be 100 nm. The TiO₂ thin dielectric film is placed on the Ti substrate at varied thickness.

The spatial field calculations are composed of two steps: the first step computes the electromagnetic field for the individual substrate without the TiO₂ dielectric, a TE polarized uniform plane wave incident at the upper port. For a periodic structure simulation, the side boundaries of the metallic Ti substrate were set with the Floquet periodic conditions, extending the geometry of the Ti film infinitely in the x-y plane. Under the Floquet boundary conditions, the mesh sizes for the opposite-coupled faces were set the same. The second step solves the total electric field ($|E|$) with the presence of TiO₂ film on the Ti substrate by applying the field

solution from the first step as the incident background field ($|E_0|$). On the second step, perfectly matched layers (PMLs) with a thickness of 100 nm were used in all the outer boundaries. To maintain the continuity between the inner simulation domain and the PML, we had split the PML domain into PMLs of blocks and assigned each block to the corresponding material of the object adjacent to it.

The normalized field intensity enhancement was calculated as a ratio of the electric field to the incident field, $|E|/|E_0|$, as a function of the wavelengths. The maximum field enhancement was calculated over the whole interface between the TiO_2 dielectric and the Ti metal substrate. The optical light absorption enhancement was determined from the ratio of the absorbed light in the substrate with and without the TiO_2 film, respectively, by using the formula below [1]:

$$f_{abs} = \omega \cdot \text{Im}(\varepsilon) \iiint |E|^2 dv$$ (1), where E(x, y, z) is the calculated electric field, and v is the volume of the corresponding geometry.

The model was solved through a parametric sweep of light wavelengths with an interval distance of 10nm. The optical constants for the materials, TiO_2 and Ti, were taken from references, respectively.[2-3] The maximum mesh size was set to 10 nm for the air domain, 2.5 nm for the TiO_2 domain, and 5 nm for the metallic Ti substrate, respectively. The maximum mesh size of 0.2 nm was used at the interface of the TiO_2 and Ti.

1.   R. A. Pala, J. White, E. Barnard, J. Liu, M. L. Brongersma, Adv. Mater. 21(2009), pp. 3504-3509.

2.   T. Siefke, S. Kroker, K. Pfeiffer, O. Puffky, K. Dietrich, D. Franta, I. Ohlídal, A. Szeghalmi, E.-B. Kley, A. Tünnermann, Adv. Opt. Mater. 4 (2016), pp. 1780-1786.

3.   W. S. M. Werner, K. Glantschnig, C. Ambrosch-Draxl, J. Phys. Chem. Ref. Data 38 (2009), pp. 1013-1092.
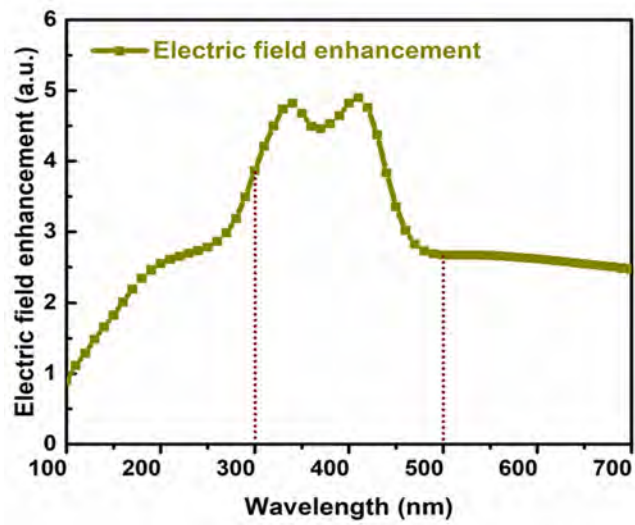
Fig. S2. Spectral maximum of the field intensity enhancement $|E|/|E0|$ at the interface between the TiO_2 dielectric and the Ti substrate. The thickness of the TiO_2 dielectric is 25 nm.
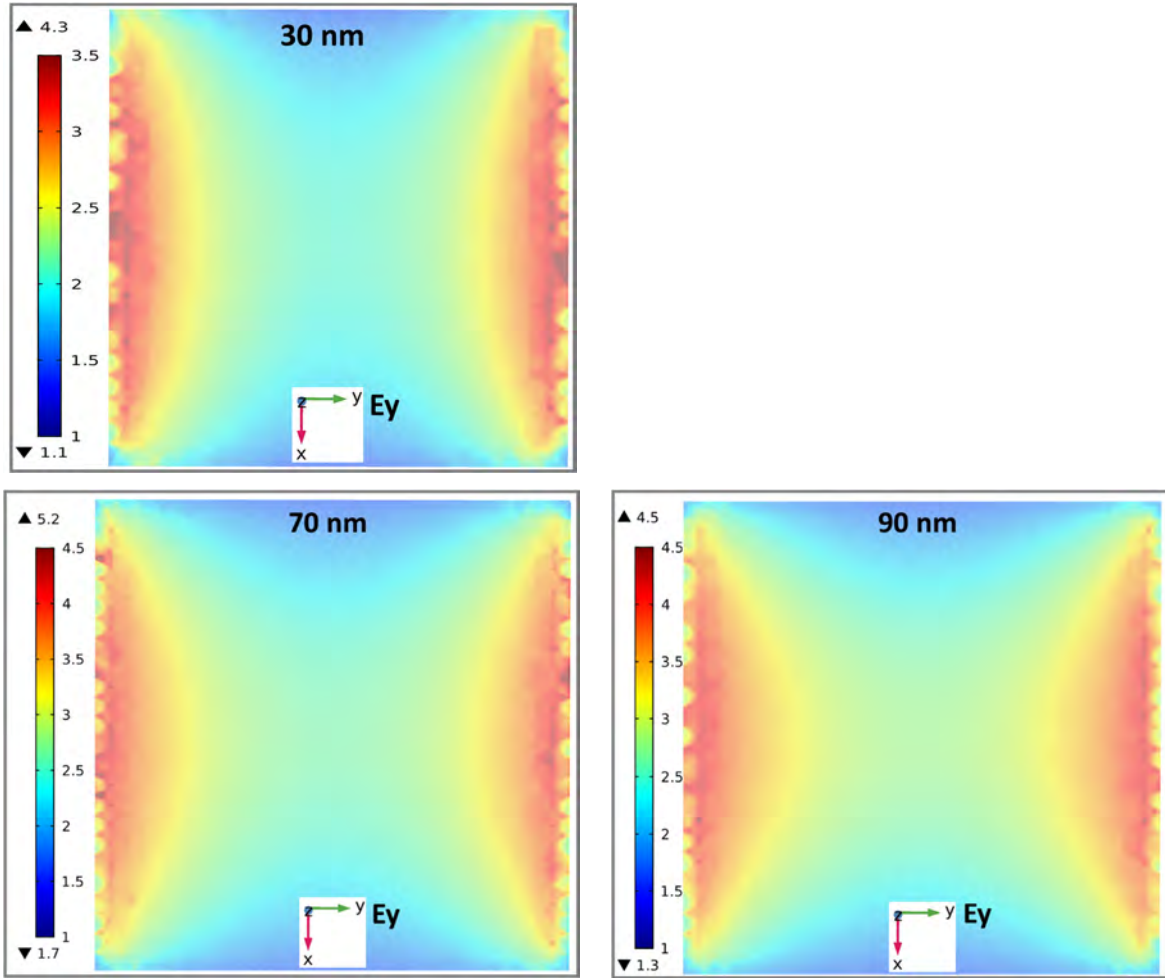
Fig. S3. Spatial field distribution |E|/|E0| at the incident electromagnetic plane wave of 450 nm with the TiO_2 dielectric film above the metallic Ti film substrate. (**a**) The width 30 nm of the metallic Ti film substrate domain in the model. (**b**) The width 70 nm of the metallic Ti film substrate domain in the model. (**c**) The width 90 nm of the metallic Ti film substrate domain in the model.

To verify if the simulated field distribution would change when the width of the geometry changes, we have simulated a set of the domains with a varied width of 30 nm, 70 nm, and 90 nm, respectively, under the polarized electric field. The periodic electric field enhancement along the polarization direction is disclosed. The width change has no impact on the enhanced field distribution, except for the field enhancement intensity. The uniformly periodic field enhancement is produced along the polarization direction. The results strongly support the significant field enhancement at the edge-interfaces of the simulated geometry.
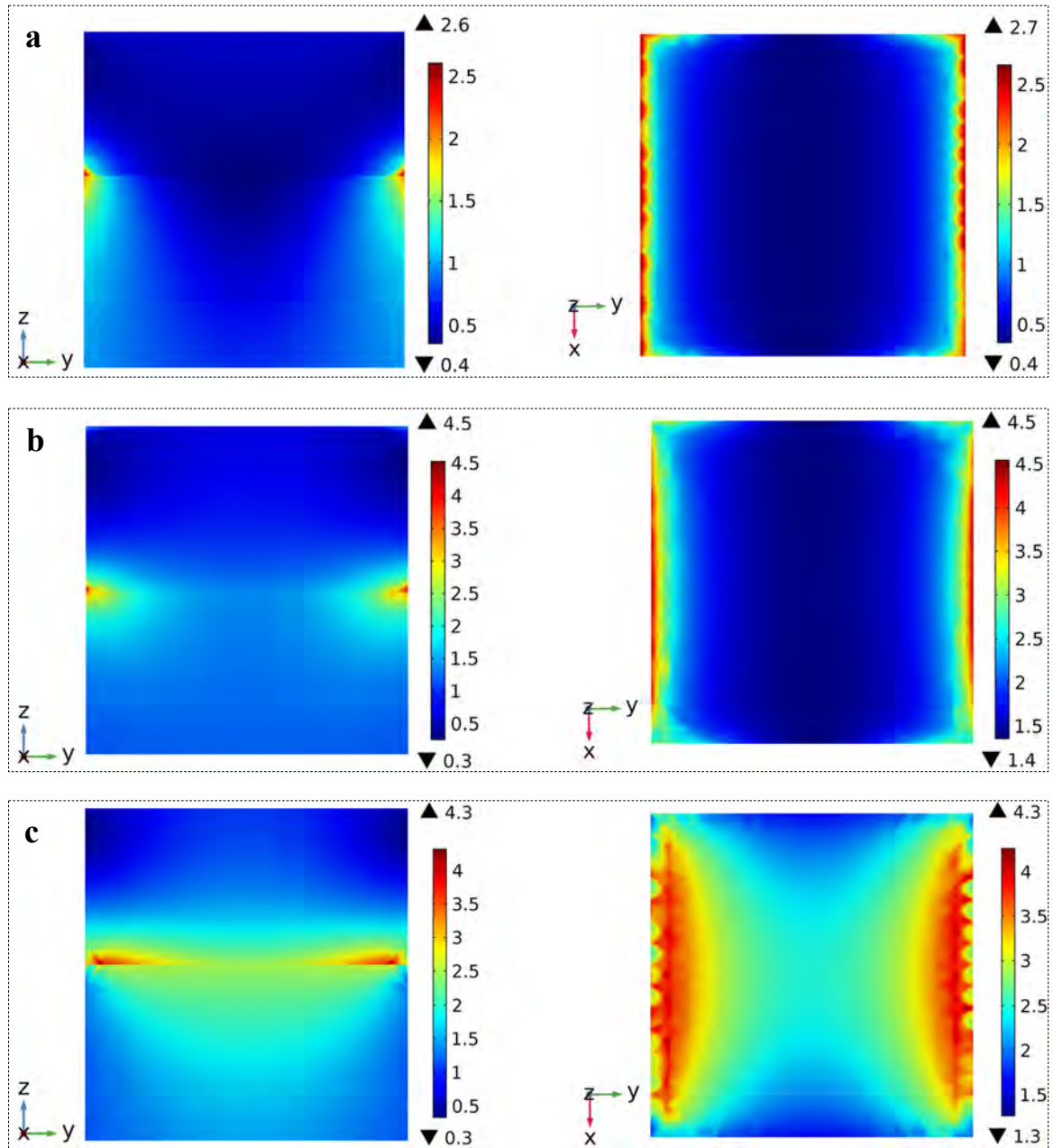
Fig. S4. Electric field profile for the surface plasmon modes on the numerical model at the three indicated wavelengths in the absorption spectrum, (**a**) 210 nm, (**b**) 380 nm, and (**c**) 450 nm; (left) in the y-z plane and (right) in the x-y plane.
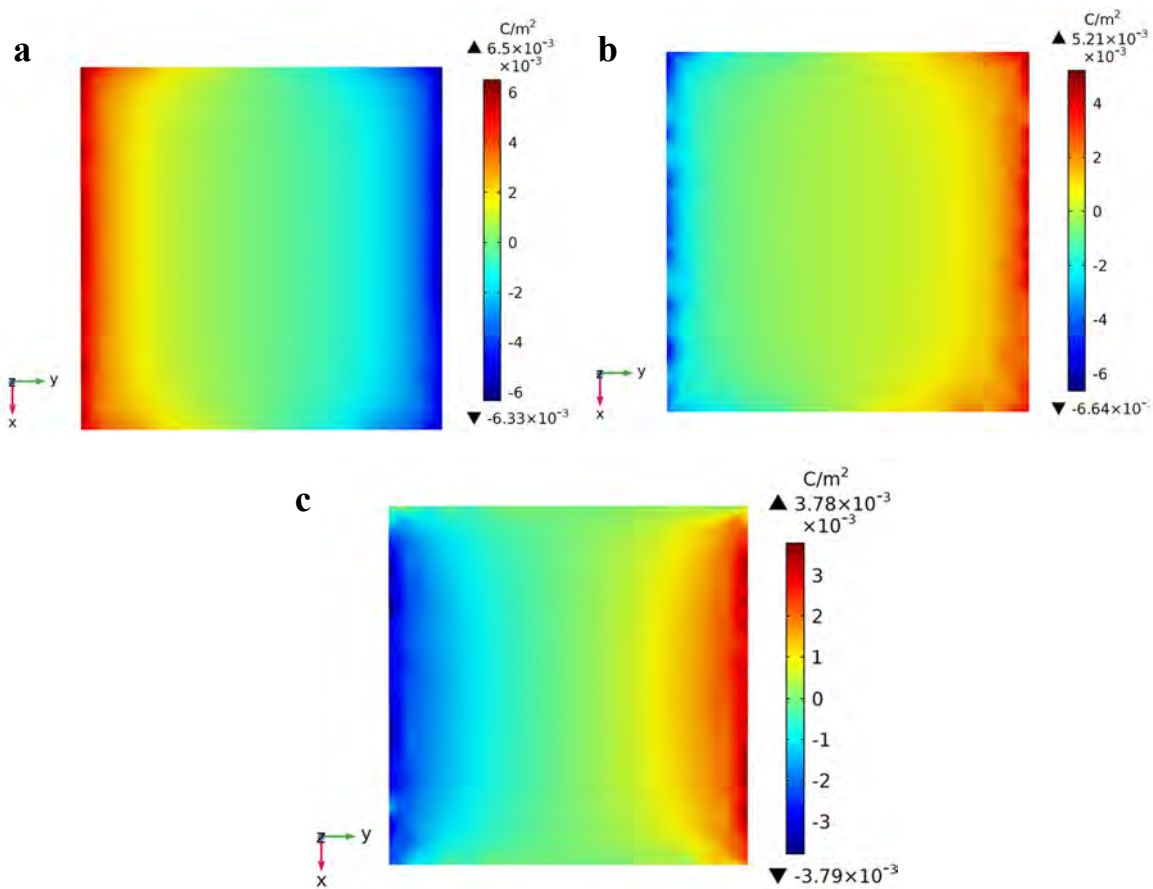
Fig. S5. Surface charge density on the interfacial surface at the three indicated wavelengths, (**a**) 210 nm, (**b**) 380 nm, and (**c**) 450 nm, in the x-y plane. The surface charge distributions were evaluated through the calculated electromagnetic fields.

The surface charge density distributions exhibit transverse dipole plasmonic modes in three patterns. At the high energy mode (210 nm), more intense charge densities are localized at the edge-interface (Fig. S5-**a**), while an opposite charge distribution is observed for the low energy mode (450 nm) (Fig. S5-**b**). At the energy of 380 nm, a hybridization of the modes results in a non-symmetrical surface charge distribution (Fig. S5-**c**). The surface charge patterns support the potentially three spectrally distinct plasmonic modes: a localized surface plasmon mode at 210 nm, a surface plasmon polariton mode at 450 nm, and a plasmon hybridization mode at 380 nm.
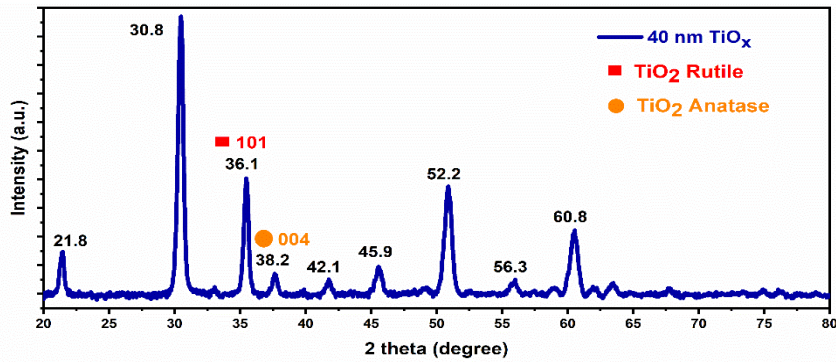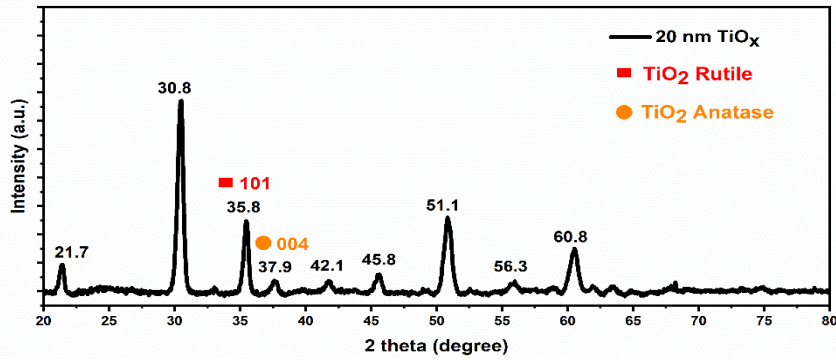
Fig. S6. XRD patterns for the two specific specimens, 20 nm TiOx/100 nm Ti/glass; 40 nm TiOx/100 nm Ti/glass. The XRD measurements were carried out at a grazing angle of 5 degrees using the apparatus of Thermo-Fisher Equinox 1000 (WL: Cu; Kα 1 = 1.54056 Å).

The XRD patterns show that the clear diffraction peaks could be assigned to the top-surface TiOx and the underneath metallic Ti materials. Peaks at about 36.0 and 38.0 degrees are assigned to the Rutile and Anatase phase of TiO_2, respectively. The peaks indicate that the as-prepared films by E-beam are crystallized in high quality after the thermal annealing.
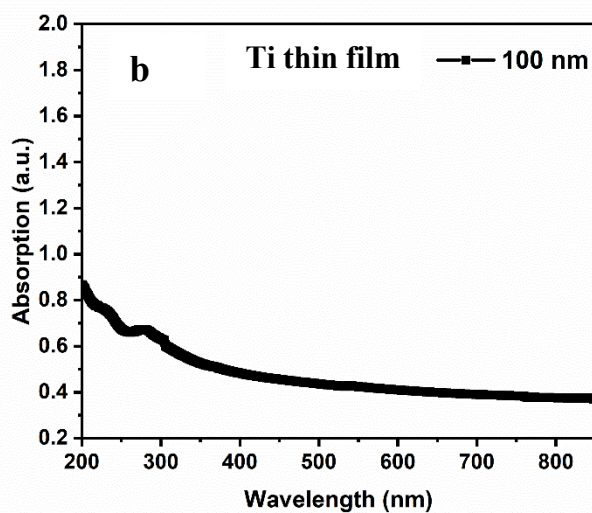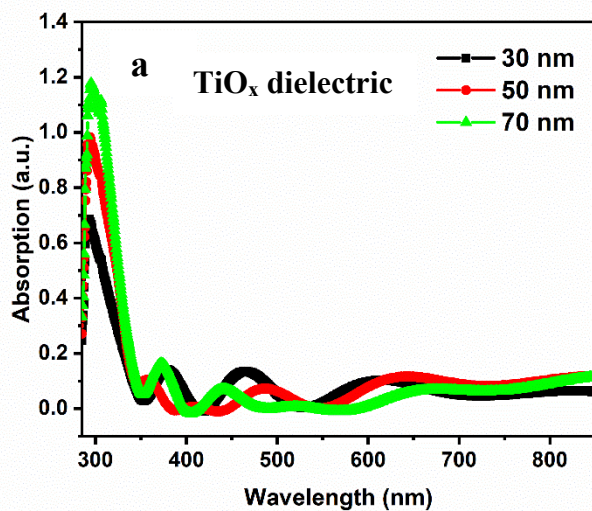
Fig. S7. The optical absorbance of (**a**) TiO_x dielectric film and (**b**) metallic Ti film, respectively, which are deposited on the glass substrate by E-beam. The absorbance spectra show that the deposited TiO_x dielectric absorbs the ultra-violet light as the typical feature of a semiconductor TiO_2 material. The interference absorption waves for TiO_x dielectric can be observed in the longer wavelengths.
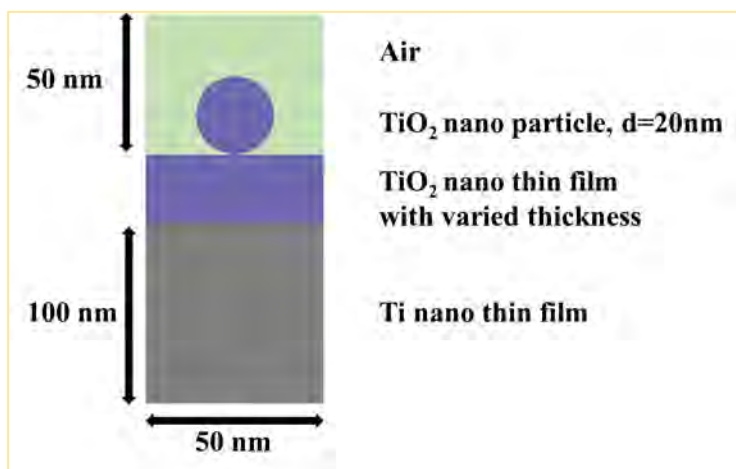
Fig. S8. Schematic of the calculation model with an introduced TiO₂ nanoparticle on the top. The radius of the TiO₂ nanoparticle is fixed to 10 nm (diameter 20 nm). The nanoparticle is placed above a TiO₂ thin film substrate. The thickness of the TiO₂ thin film is varied in the calculations.
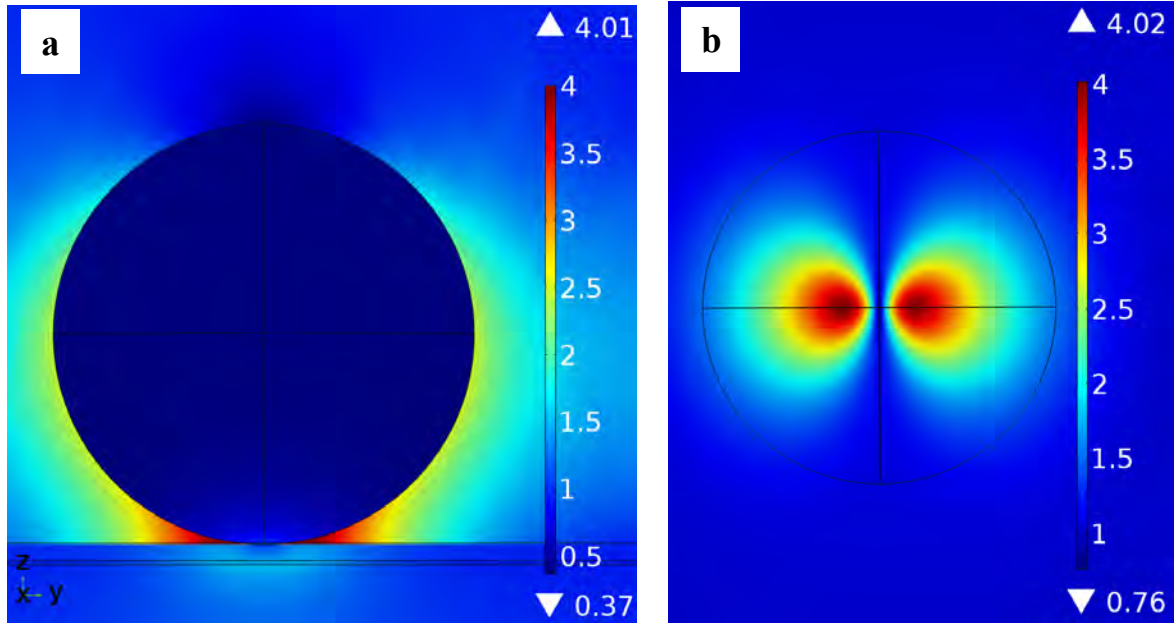
Fig. S9. Spatial field distribution |E|/|E0| at the incident electromagnetic plane wave of 430 nm with the dielectric nanoparticle of TiO_2 placed on 1 nm thickness TiO_2 thin-film dielectric above the Ti metal substrate. (**a**) Spatial field distribution in the z-y plane. (**b**) Spatial field distribution in the x-y plane.
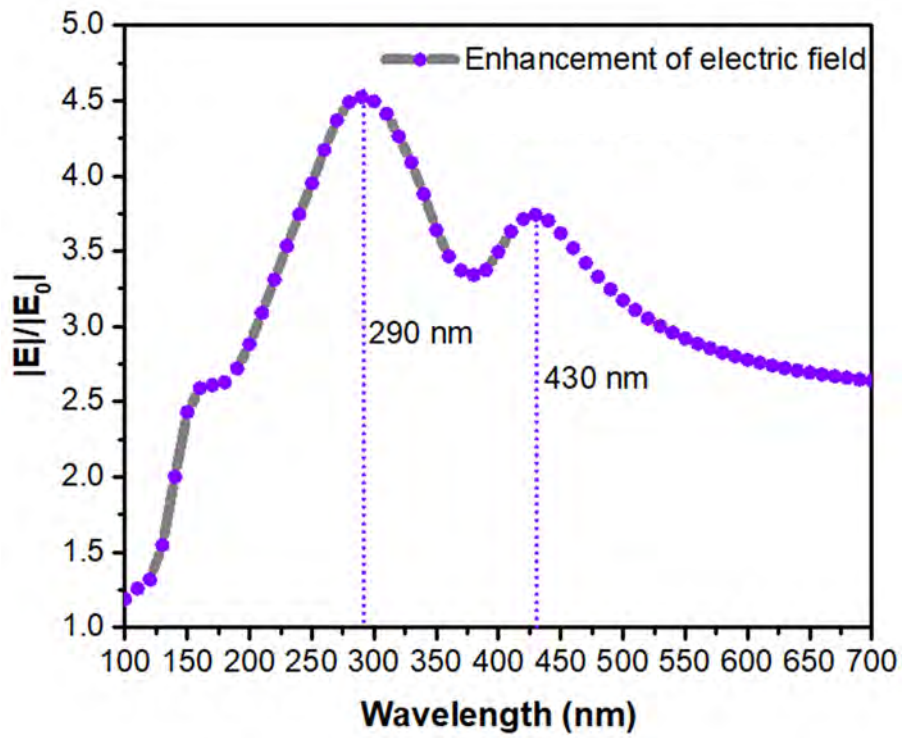
Fig. S10. Spatial field enhancement |E|/|E₀| as a function of incident light wavelengths for the dielectric particle of TiO$_2$ placed over the Ti metal substrate, with 1 nm TiO$_2$ thin dielectric film in the middle.
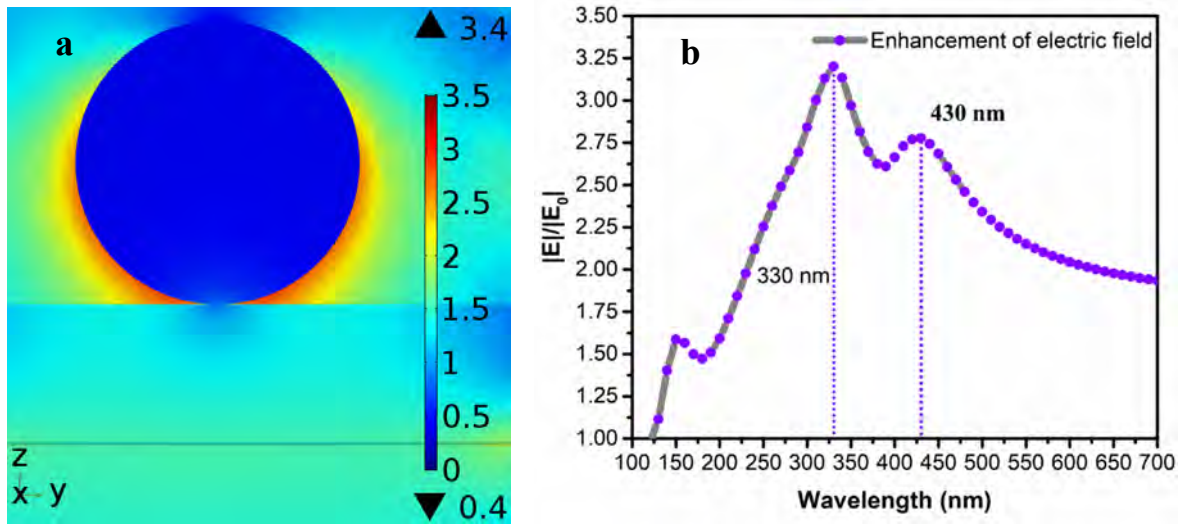
Fig. S11. Calculated field distribution and enhancement with the 10 nm thickness of the TiO_2 thin dielectric film. (**a**) Spatial electric field distribution in the y-z plane at 430 nm with 10nm TiO_2 thin film dielectric in the middle between the NP and Substrate. (**b**) Corresponding spatial electric field enhancement $|E|/|E_0|$ as a function of incident light wavelengths for the dielectric particle of TiO_2 placed over the Ti metal substrate, with 10 nm TiO_2 thin dielectric film in the middle.
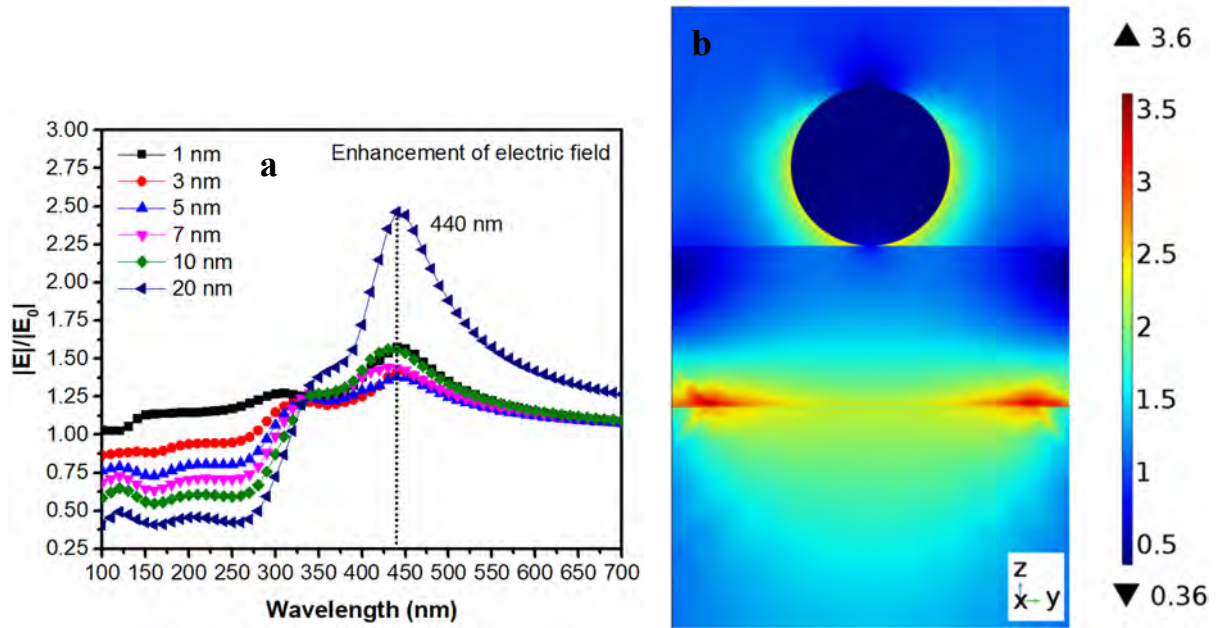
Fig. S12. Spatial electric field enhancement |E|/|E₀| and spatial distribution with dielectric nanosphere particle of TiO_2 placed on 20 nm TiO_2 dielectric film over a Ti metal substrate. (**a**) Electric field enhancement as a function of the defined thickness of the TiO_2 dielectric film. The enhancement peaks center at about 440 nm. (**b**) Corresponding spatial field distribution in the y-z plane at the incident plane wave of 440 nm.

Fig. S13. Schematic illustration of the fabrication processes for the Ti-TiO$_x$ film composites on a plane substrate of silicon. The metallic Ti film was deposited by E-beam. The thickness of the flat Ti film is 300 nm, with the roughness of Ra: 84 nm; Rq: 255 nm, on the substrate of silicon. The as-deposited Ti was followed by the various thermal oxidation temperatures (400, 450, 500, 550, 600, 650 °C) for 5 h in a tube furnace with the controlled flowing of oxygen gas. The roughness was measured by the interferometer (Wyko NT9100).
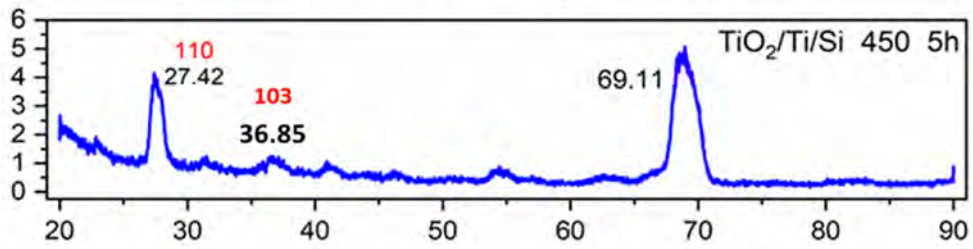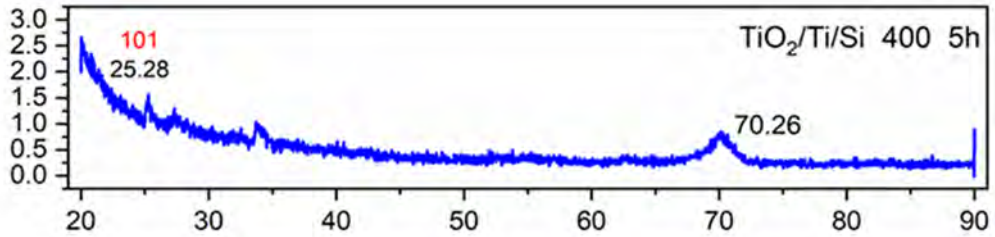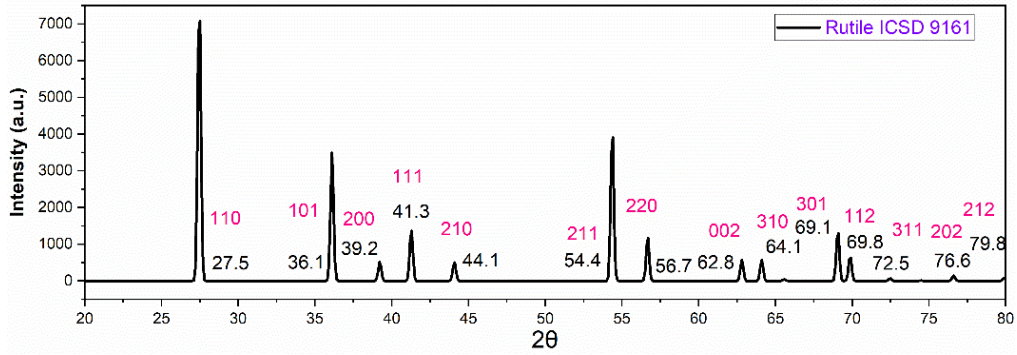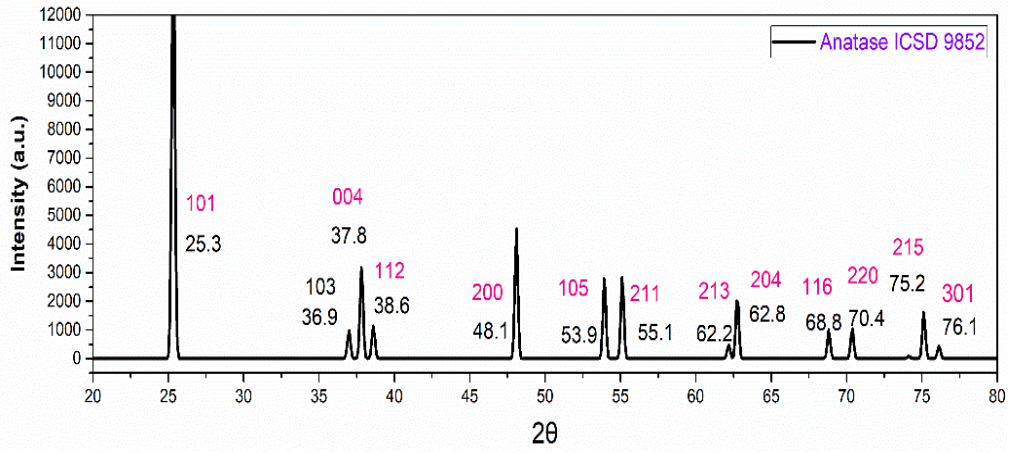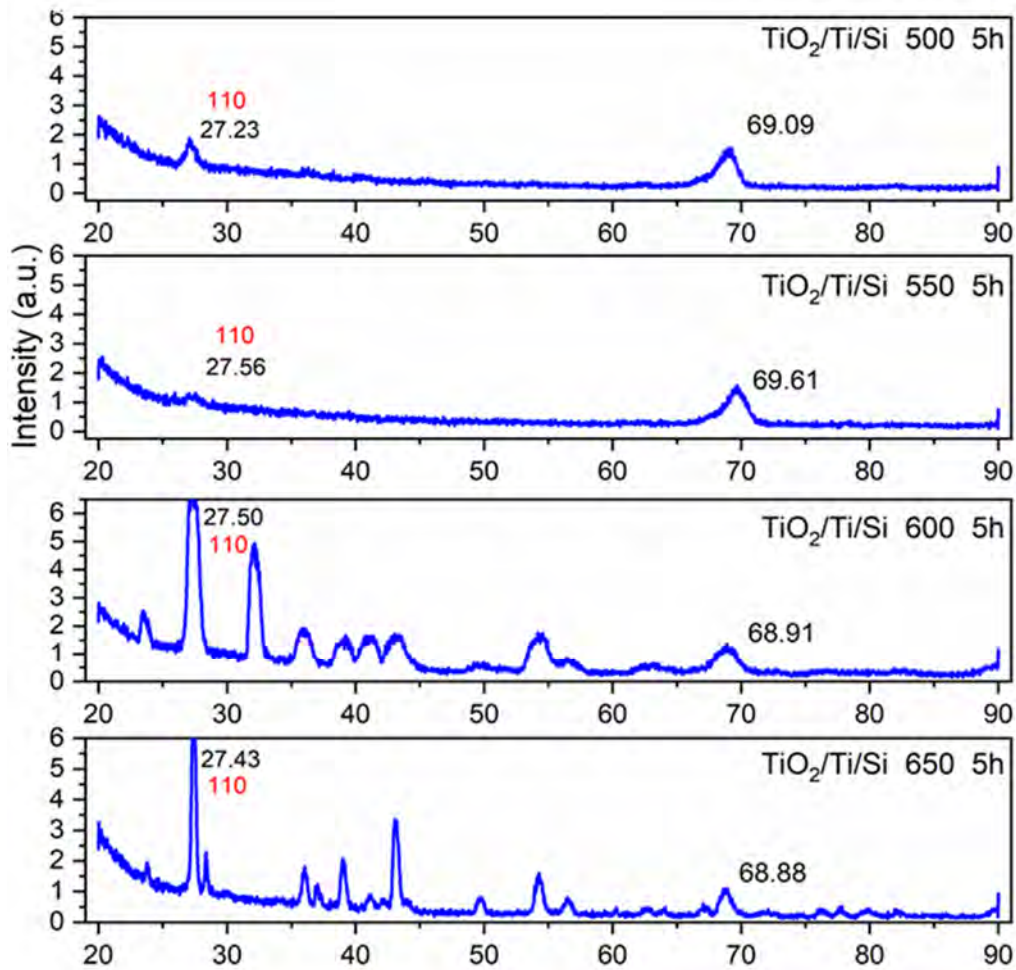
Fig. S14. XRD patterns for the as-prepared specimens (400, 450, 500, 550, 600, 650 °C), with the referred pdf cards of TiO_2. The XRD measurements were carried out at a grazing angle of 1.5 degrees using the apparatus of Bruker D8 (WL: Cu; Kα 1 = 1.54056 Å).

With the higher temperatures, the intensity of the peaks are becoming stronger in the patterns. The overall low intensity indicates that the sub-oxidized TiO_x dielectric layer is developed on the metallic Ti surface. The individual weak peaks assigned to TiO_2 are emerged after the thermal sub-oxidation process, indicating that the TiO_x dielectric is formed on the surface.
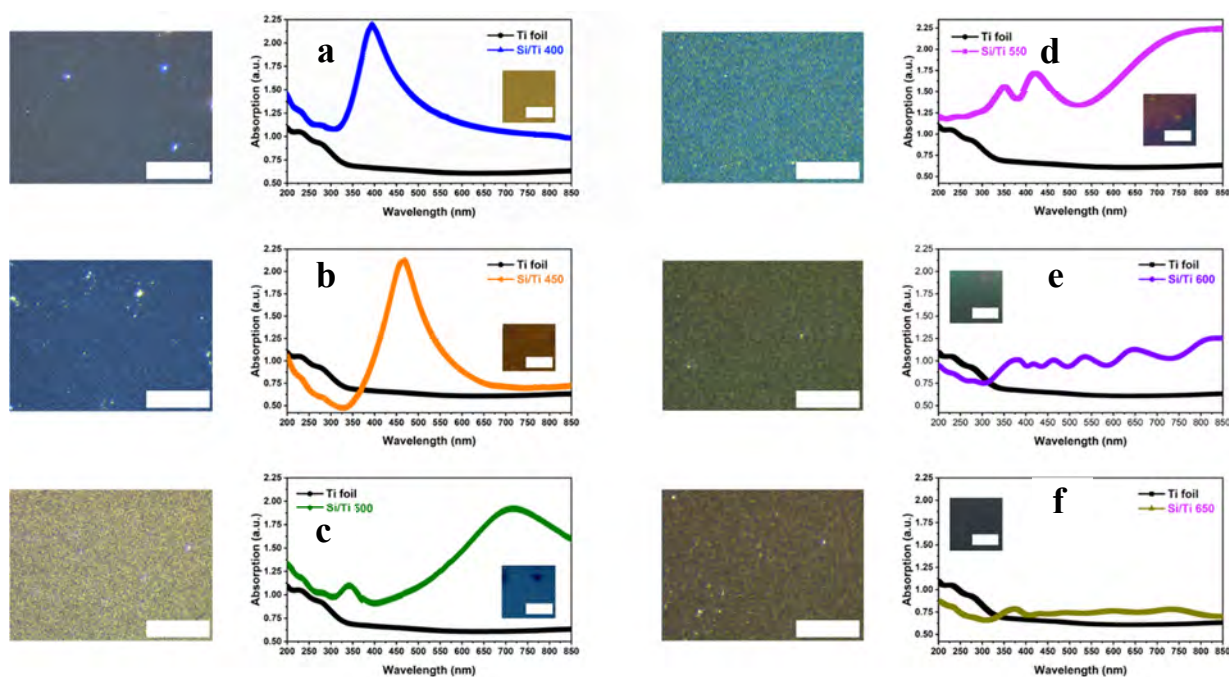
Fig. S15. Absorption spectra of the Si/Ti/TiO$_x$, (**Si/Ti**; **a**: 400, **b**: 450, **c**: 500, **d**: 550, **e**: 600, **f**: 650 °C) with dark-field optical scattering images on the left (scale bar: 30 μm). The insets are corresponding bright-field images (scale bar: 3.0 mm). The colors of dark-field images are highly in line with the wavelength color of the absorbed visible light, complementary to the colors of bright-field images. The absorption spectra of pure flat Ti foil without any surface patterns are added as a reference. At lower points of the temperatures (400, 450, 500 °C), resonant absorption peaks are obtained in the wavelength range of 300-500 nm, which we attribute to the plasmon-induced absorption enhancement. The red-shifting of the peaks is due to the change of the surface dielectric properties after the varied high temperature. The tunable resonant absorption peak in the visible light range is highly controlled with the adjustment of sub-oxidation temperature. The shifting confirms that the excitation of plasmon resonance can be achieved by sub-oxidizing the Ti metal film with a suitable temperature.
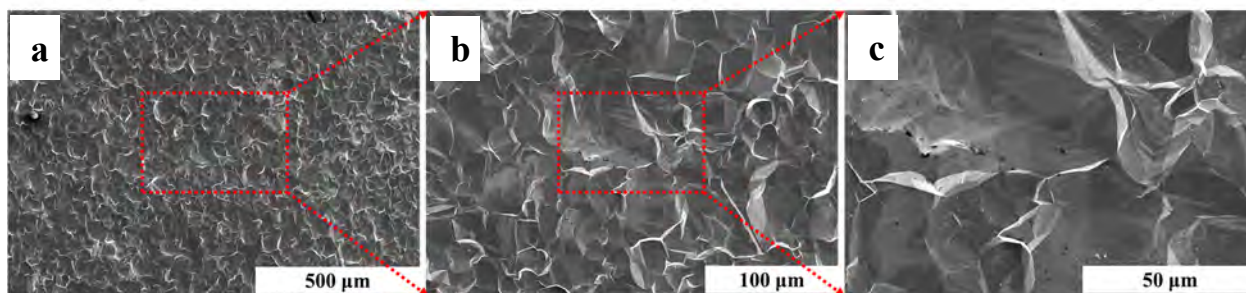
Fig. S16. SEM images of the as-etched surface nanostructures on the Ti foil before the thermal sub-oxidation process. After the chemical etching, the surface shows the quasi-patterned nano-crystalline quasi-prisms structures. The rich edge-interfaces at the nano-prisms provide a density of hot-spots on the surface for scaling-up the plasmon resonance performance. The insets are corresponding scale bars.
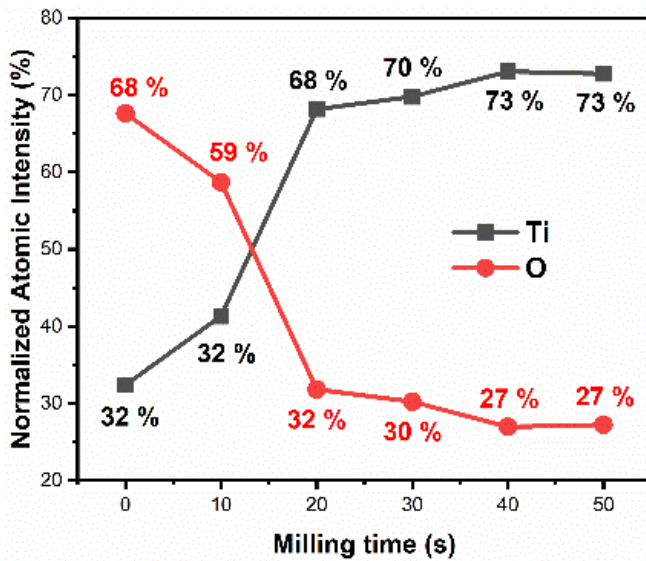
Fig. S17. Surface elemental composition (normalized) obtained from XPS survey spectrum.

We have performed X-ray photoelectron spectroscopy (XPS) measurements. XPS is a beneficial technique to identify chemical species at the surface or in the depth-direction through the observation of peak positions and peak shapes.

The depth profile shows a gradual decline of oxygen content and an increase in titanium content. In the depth direction, the oxygen never goes down to zero, because the XPS is highly sensitive to the surface roughness.

At the initial time period, TiO_2 with the ratio of titanium to oxygen atoms is present close to the theoretical value. Also, the Oxygen peak (529.3 eV) and Titanium (458.1 eV) peak are not shifted from literature values[1] when referenced to the adventitious C1s peak at 284.8 eV. These results strongly support that TiO_2 is formed on the top surface after the thermal process. Sub-oxidized titanium oxide and metallic titanium are both formed and constructed underneath the TiO_2 dielectric.

1. J. Zheng, Y. Lyu, R. Wang, C. Xie, H. Zhou, S.P. Jiang, S. Wang, Nat. Commun., 9 (2018), pp. 3572.
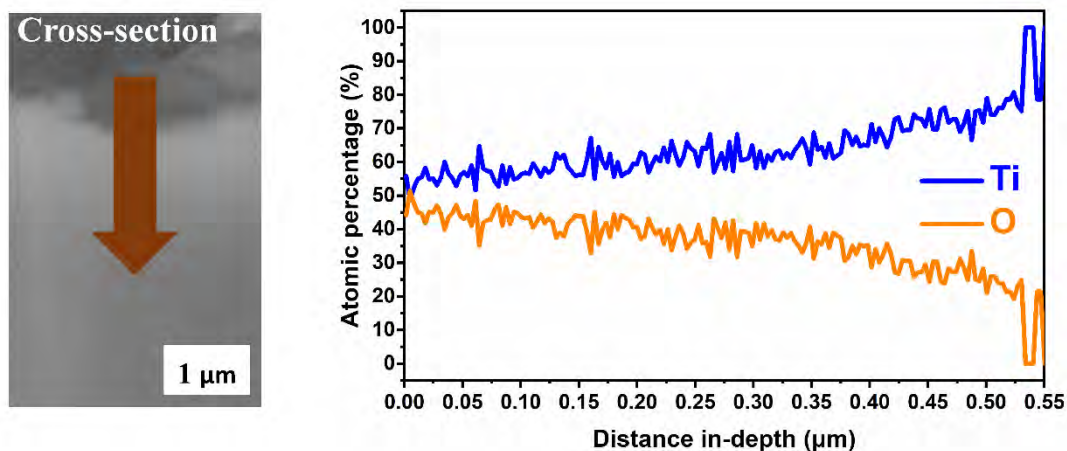
Fig. S18. Cross-sectional analysis of the sub-oxidized Ti foil with Ti-TiO$_x$ nanostructure composites, the cross-sectional image (left), and the quantitative analysis of the elements along the arrow direction (right).[1] Ultra-high-resolution FE-SEM with EDS (SU8230) was used for the analysis.

In the depth-direction, a gradual decrease of the oxygen is disclosed, with a gradual increase of the Ti element. After the sub-oxidation process, oxygen elements are introduced from the top surface to the interior Ti metal substrate, forming low-value titanium oxides on the top surface layer. The chemical states consist of a sandwich composition, top-surface TiO$_2$ layer, low-value TiO$_x$ oxides middle-layer, and O-Ti solid bottom-layer. These revealed chemical states are consistent with the reported investigations.[2-4] Thus, top-surface Ti-TiO$_x$ composites are formed after the sub-oxidation process.

1. C. Cheng, M.N. Akram, O. Nilsen, N. Pryds, K. Wang, *Phys. Chem. Chem. Phys.*, 22 (2020), pp. 7769-7777.

2 J.W. Rogers, K.L. Erickson, D.N. Belton, R.W. Springer, T.N. Taylor, J.G. Beery, Appl. Surf. Sci., 35 (1988), pp. 137-152.

3 G. Lu, S.L. Bernasek, J. Schwartz, Surf. Sci., 458 (2000), pp. 80-90.

4 Y. Horio, Y. Hara, Y. Yamamoto, Y. Morimoto, T. Naitoh, Jpn. J. Appl. Phys., 51 (2012).
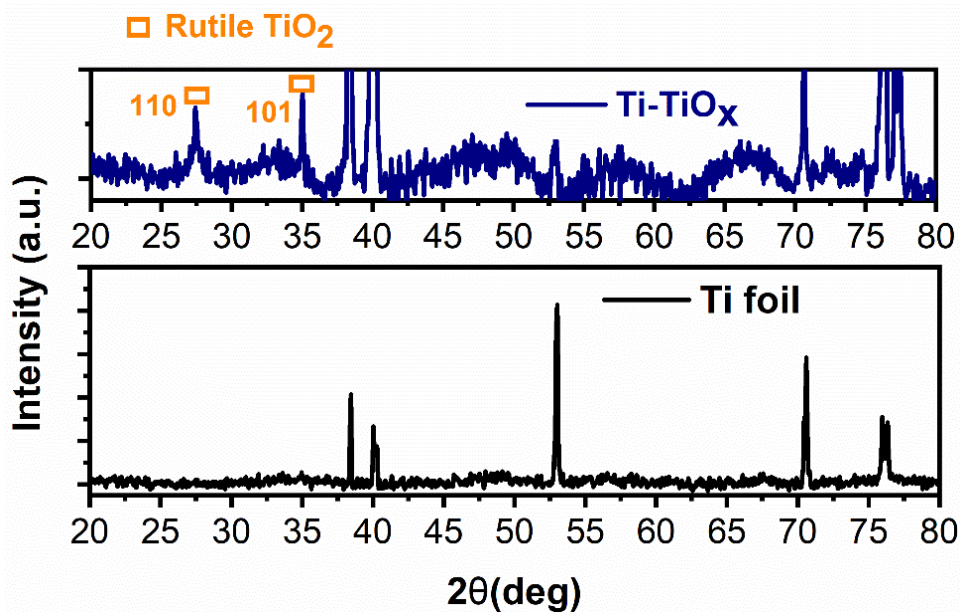
Fig. S19. XRD patterns for the specific specimens of the sub-oxidized Ti foils. The XRD measurements were carried out at a grazing angle of 1.5 degrees, on the apparatus of Bruker D8 (WL: Cu; Kα 1 = 1.54056 Å).

In the XRD patterns, the peaks centered at 27.5 and 36.1 are assigned to the Rutile TiO_2 in referring to the pdf card of Rutile ICSD 9161. The peaks at higher degrees are aligned with the peaks in the XRD patterns of the Ti foil. The XRD data shows that the surface Ti is sub-oxidized into TiO_x after the sub-oxidation process.
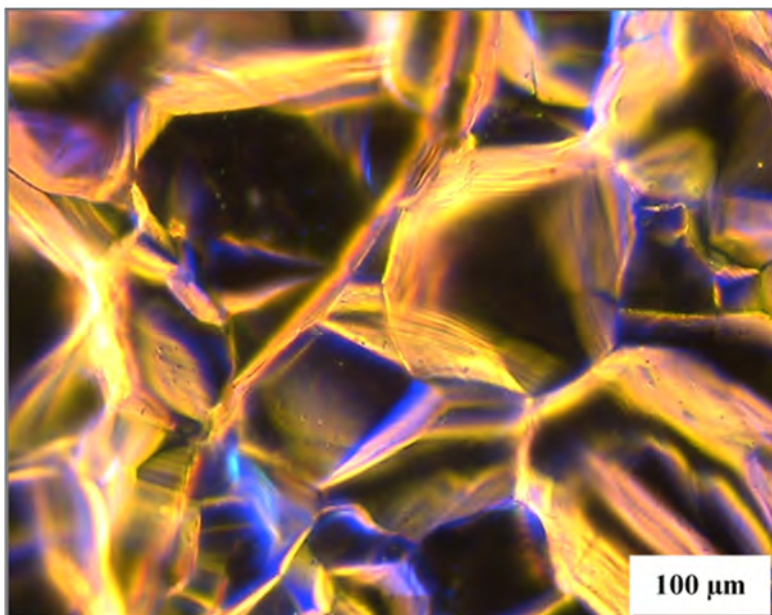
Fig. S20. Dark-field optical images of the as-prepared nanocomposite of Ti-TiO$_x$ nanostructures after the thermal sub-oxidation. The inset scale bar is 100 μm.
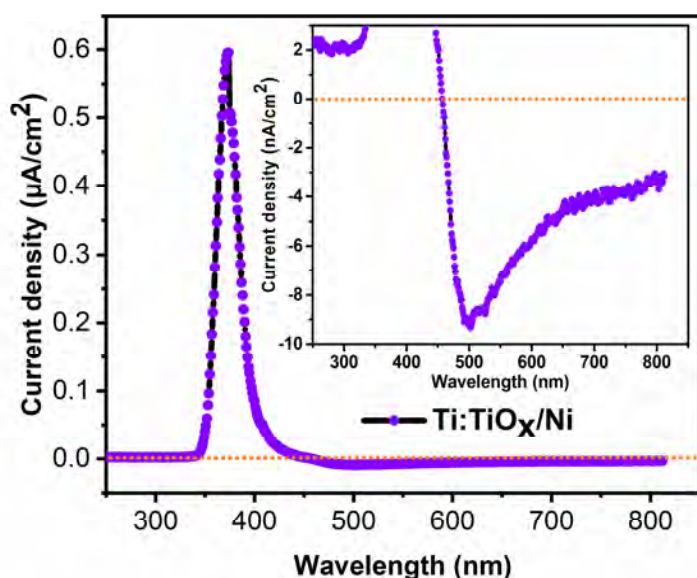
Fig. S21. The IPCE action spectrum of the as-prepared nanocomposite of the Ti-TiO$_x$ nanostructures, which was applied as a photoanode in a 3-electrodes configuration cell with 1 M KOH liquid electrolyte solution. The positive-sign of current indicates the photochemical activity of water oxidation reactions. In contrast, the negative-sign of the current indicates the photoelectrochemical reduction reactions activated on the photoelectrode under the specific light illumination. The inset is the magnification of the IPCE activity in the corresponding light wavelengths range.

Photo-corrosion induced instability is usually encountered by TiO$_x$-based photoanodes[1]. Thus, we applied an ultra-thin Ni film layer to prevent the photoelectrode Ti-TiO$_x$ from corrosion. The protection material for the photoelectrode should possess favorable and stable optical, electronic, and chemical properties that benefit the designed redox reactions and ideally function as a catalyst or co-catalyst for the reaction of interest[2]. In this study, Ni offers corrosion resistance, high stability, and Earth abundance, making it a superior candidate material.

1. Y. Yang, Y. Ling, G. Wang, T. Liu, F. Wang, T. Zhai, Y. Tong and Y. Li, Nano Lett., 15 (2015), pp. 7051-7057.

2. S. Hu, Nathan S. Lewis, J. W. Ager, J. Yang, J. R. McKone, N. C. Strandwitz, J. Phys. Chem. C, 119 (2015), pp. 24201-24228.